Scholar Commons
USF University of South Florida

University of South Florida
Scholar Commons

Graduate Theses and Dissertations | Graduate School

June 2018

Quantitative Measurement of Cerebral Hemodynamics During Activation of Auditory Cortex With Single- and Multi-Distance Near Infrared Spectroscopy

Penaz Parveen Sultana Mohammad
University of South Florida, pmohammad@mail.usf.edu

Follow this and additional works at: https://scholarcommons.usf.edu/etd

 Part of the Electrical and Computer Engineering Commons

Scholar Commons Citation
Mohammad, Penaz Parveen Sultana, "Quantitative Measurement of Cerebral Hemodynamics During Activation of Auditory Cortex With Single- and Multi-Distance Near Infrared Spectroscopy" (2018). *Graduate Theses and Dissertations.*
https://scholarcommons.usf.edu/etd/7698

This Thesis is brought to you for free and open access by the Graduate School at Scholar Commons. It has been accepted for inclusion in Graduate Theses and Dissertations by an authorized administrator of Scholar Commons. For more information, please contact scholarcommons@usf.edu.

المنارة للاستشارات

www.manaraa.com

Quantitative Measurement of Cerebral Hemodynamics During Activation of Auditory Cortex With Single- and Multi-Distance Near Infrared Spectroscopy

by

Penaz Parveen Sultana Mohammad

A thesis submitted in partial fulfillment
of the requirements for the degree of
Master of Science in Electrical Engineering
Department of Electrical Engineering
College of Engineering
University of South Florida

Major Professor: Ashwin B Parthasarathy, Ph.D.
Andrew Hoff, Ph.D.
Ann Eddins, Ph.D.

Date of Approval:
June 13, 2018

Keywords: Absolute concentration, fNIRS, Modified Beer-Lambert law, FD-DOS, Functional activation

Copyright © 2018, Penaz Parveen Sultana Mohammad

www.manaraa.com

DEDICATION

To my family for their support and faith in me and to Dr. Ashwin B Parthasarathy for his support and guidance.

www.manaraa.com

ACKNOWLEDGMENTS

I would like to acknowledge the support given by my advisor Dr. Ashwin B Parthasarthy. Dr. Parthasarathy was a great mentor and was always encouraging and appreciative. I would like to thank him for the patience he has shown for making me understand the trivial concepts. I also acknowledge the efforts by Dr. Ann Eddins and Pound for their crucial help during the data collection. I truly appreciate Dillon Buffone for his help with 3D printing of the probe.

I would like to thank my fellow lab mates and friends including Sadhu Moka, Shraddha Pandey, Shreyas Shivanna, Arindam Biswas, Pavia Bera, Abdul Safi, Bradley Shaw, Nikola Otic and Riditha Rahman Khan for creating a supportive environment and for kindly agreeing to participate in the experiments. A great deal of thanks to all the cheerful test subjects for helping me make this thesis successful.

Finally I would like to thank my parents and family for their faith in me and for their guidance in everything I pursued.

www.manaraa.com

TABLE OF CONTENTS

www.manaraa.com

www.manaraa.com

LIST OF TABLES

www.manaraa.com

LIST OF FIGURES

www.manaraa.com

www.manaraa.com

ABSTRACT

Functional Near Infrared Spectroscopy (fNIRS) is a safe, low-cost, non-invasive optical technique to monitor focal changes in brain activity using neurovascular coupling and measurements of local tissue oxygenation, *i.e.,* changes in concentrations of oxygenated hemoglobin (HbO) and deoxygenated hemoglobin (HbR)[42]. This thesis utilizes two fNIRS approaches to measure hemodynamic changes associated with functional stimulation of the human auditory cortex. The first approach, single-distance continuous wave NIRS (CW-NIRS) utilizes relatively simple instrumentation and the Modified-Beer Lambert (MBL) law to estimate activation induced *changes* in tissue oxygenation (ΔC_{HbO} and ΔC_{HbR})[17]. The second more complex approach, frequency domain NIRS (FD-NIRS), employs a photon diffusion model of light propagation through tissue to measure both baseline (C_{HbO} and C_{HbR}), and stimulus induced changes in oxygenated and deoxygenated hemoglobin[10]. FD-NIRS is more quantitative, but requires measurements at multiple light source-detector separations and thus its use in measuring focal changes in cerebral hemodynamics have been limited.

A commercial FD-NIRS instrument was used to measure the cerebral hemodynamics from the right auditory cortex of 9 adults (21 ± 35 years) with normal hearing, while presented with two types of auditory stimuli: a 1000 Hz Pure tone, and Broad band noise. Measured optical intensities were analyzed using both MBL and photon diffusion approaches. Oxygenated hemoglobin was found to increase by 0.351 ± 0.116 μM and 0.060 ± 0.084 μM for Pure tone and Broad band noise stimuli, when analyzed by the MBL method at the

www.manaraa.com

'best' source-detector separation. On average (across all sources), MBL analysis estimated an increase in C_{HbO} of 0.100 ± 0.075 μM and 0.099 ± 0.084 μM respectively for Pure tone and Broad band noise stimulation. In contrast, the frequency domain analysis method estimated C_{HbO} to increase by -0.401 ± 0.384 μM and -0.031 ± 0.358 μM for Pure tone and Broad band noise stimulation respectively. These results suggest that although more quantitative, multi-distance FD-NIRS may underestimate focal changes in cerebral hemodynamics that occur due to functional activation. Potential reasons for this discrepancy, including the partial volume effect, are discussed.

www.manaraa.com

CHAPTER 1: INTRODUCTION

Functional activation is a powerful non-invasive technique for the in-vivo characterization of specific neuronal circuit/organization/activity in the brain. In humans, these experiments involve the stimulation/activation of sensory and/or motor neuron clusters, and the non- invasive measurement of corresponding electro physiological or hemodynamic responses [15, 42, 22]. Functional characterization of motor neurons via finger tapping is a classic example. Here, the subject 'taps' their thumb and index finger at a predetermined rate (usually ~ 3 Hz), which activates the corresponding neurons in the motor cortex. The physiological effects of this activation is then characterized by measuring the electrical/hemodynamic response. Several imaging/monitoring modalities have been used over the decades to study the functional activity in the brain. Techniques such as Electroencephalography (EEG) [11, 37] directly measure the electrical de-/re-polarizations of the neurons, while methods such as functional Magnetic Resonance Imaging (fMRI)[16] Single photon emission computed tomography (SPECT) [28], Positron emission tomography (PET) [34], Computed tomography(CT) [33], and Near-Infrared Spectroscopy (NIRS) [43, 27, 11] measure the hemodynamic (*i.e.,* blood flow/blood oxygenation) changes associated with neuronal activation (*i.e.,* via neurovascular coupling [38, 22]).

In this thesis we characterize the functional hemodynamic response from the auditory cortex, with a long-term goal to investigate the differences in auditory hemodynamic re-

www.manaraa.com

sponses from individuals with, and without tinnitus. Tinnitus is a common hearing problem that effects 1 in 10 people in the United States [5]. Tinnitus refers to the perception of 'noise' or 'ringing' in the ears, and could signify underlying hearing conditions such as hearing loss or ear injury. Some recent studies have shown increased functional activity in regions of auditory cortex in people suffering with tinnitus compared to those without tinnitus [39, 27]. It is generally difficult to measure hemodynamic response to activations of the auditory cortex with clinical imaging modalities such as fMRI or CT, because instrument sounds can corrupt/influence presentation of auditory stimuli to the subjects. In this context, the optical technique of Near Infrared Spectroscopy (NIRS) provides an effective, silent and non invasive way to measure hemodynamic responses from controlled stimulation of the auditory cortex. NIRS has several other inherent advantages. First, optical imaging modalities have significantly low setup and operating costs. Second, optical imaging methods are portable and easy to use, making it an ideal choice for bedside monitoring. Finally, optical irradiation is non-ionizing and safe to use.

NIRS estimates the concentrations of oxygenated/deoxygenated hemoglobin (and hence tissue oxygen saturation), from the differential absorption of light of different wavelengths by components of tissue (*e.g.,* oxy- or deoxy- hemoglobin, lipids, water). The most common and simplest implementation of NIRS is Continuous Wave Near-Infrared Spectroscopy (CW-NIRS), where tissue is illuminated by multi-wavelength near-infrared light of constant (*i.e.,* continuous) intensity. The absorbance/attenuation of the diffusely reflected light is measured, and changes in oxygenated and deoxygenated hemoglobin is estimated by the modified Beer-Lambert law [9, 3, 17]. CW-NIRS thus offers a fast and convenient method for measuring functional changes, with several studies utilizing commercial NIRS instruments to

www.manaraa.com

characterize stimulation of the auditory cortex [27, 24, 11, 43]. For example Chen et.al. [11], used a NIR Scout 816 (NIRx Medical Technologies, LLC) device to study the responses of the auditory cortex for 2 different types of sounds: pure-tone at 440 and 554 Hz and a 1000 Hz frequency modulated wave that produced a 'warbling Sound'. Hong and Santosa [24] used DYNOT (NIRx Medical Technologies, LLC) to study the hemodynamic responses of the auditory cortex for four different types of sound categories, which included English, Non-English, annoying and nature sounds. Notably, all these studies utilize CW-NIRS and the Modified Beer-Lambert (MBL) law which only nominally accounts for scattering of light in tissue [11], and can only measure relative changes in the concentration of oxygenated hemoglobin (HbO) and deoxyenated hemoglobin (HbR).

A second, and more quantitative approach to measuring cerebral hemodynamics is Frequency Domain NIRS (FD-NIRS), which utilize intensity modulated light of different near-infrared wavelengths to derive both tissue absorption and tissue scattering properties. Here, tissue is illuminated with light, the intensity of which is modulated sinusoidally (~ 100 MHz), and the phase and amplitude changes of light propagated through tissue (with respect to illumination) is measured at different source-detector separations. When combined with a photon diffusion model, the simultaneously measured amplitude and phase changes permit quantification of both tissue absorption and scattering coefficients. However, although FD-NIRS has been used to measure absolute changes in the HbO and HbR concentrations in the brain [12, 21, 10, 31], they have primarily focused on *global* changes such as hypoxia and cerebral ischemia. Indeed, there is very little literature on the use of these quantitative techniques for functional activation experiments to measure *focal* changes in absolute concentrations of HbO, HbR.

www.manaraa.com

1.1 Research Question

The goal of this thesis is to measure the absolute (*i.e,* baseline) as well as relative changes in *HbO* and *HbR* during the functional activation of the auditory cortex with FD-NIRS and CW-NIRS respectively. We use a commercial frequency domain NIRS system (Imagent, ISS inc., IL, USA) to measure the functional activation over the auditory cortex region. Relative changes in *HbO* and *HbR* concentrations are calculated using the modified Beer-Lambert law, under the assumption that light scattering increases the path length of light traveled in tissue by a constant value. Note that the Modified Beer-Lambert (MBL) analysis uses the Ac component and/or the DC component of the light fluence rate (*i.e.,* intensity) measured from the Imagent system. Absolute (*i.e.,* baseline) values of *HbO* and *HbR* concentrations are calculated by quantitatively measuring the tissue absorption and scattering coefficients. This is accomplished by measuring both amplitude and phase changes (w.r.t a reference) collected from the FD-NIRS system. Measured amplitude and phase permit full characterization of the photon diffusion through tissue thus enabling quantitative measurements. We analyze and compare the results obtained from both analysis methods for 9 subjects and identify and discuss the inconsistencies in the results.

1.2 Thesis Organization

The remainder of this thesis is organized thusly. Chapter 2 provides the underlying fundamentals of different NIRS approaches and the mathematics involved for these measurements. The different types of optical sources, the assumptions made therein for the consideration of the measurement geometry, and different analysis techniques are elaborately discussed. Chapter 3 discusses the technical details and experimental methodology

www.manaraa.com

of the system. The experimental set up and protocol used for the measurements in this thesis, including instrument description, the type stimuli presented, technical details of the fiber-optic probe and the positioning of the probe are described. A flow chart is provided for the both analysis methods. Chapter 4 summarizes the results obtained for the different types of stimuli used and for the two different analysis techniques. The results from the two analysis techniques is compared for their consistency(or)inconsistency. The challenges faced during the experiments are also discussed. Finally, chapter 5 presents concluding thoughts of this research and discusses future work.

www.manaraa.com

CHAPTER 2: FUNDAMENTALS OF DIFFUSE OPTICAL SPECTROSCOPY

2.1 Tissue Spectroscopy

Diffuse optical spectroscopy (DOS) is a low cost optical technique to quantitatively measure tissue chromophore concentrations. More specifically, DOS characterizes the propagation of light through tissue and measures/estimates tissue optical properties, *i.e.,* absorption and scattering coefficients. Absorption refers to the transfer of energy from light to (typically) heat in tissue. Scattering refers to the change in direction of propagation of light due to (typically elastic) collision with tissue components such as cells. Thus, tissue light scattering has the effect of increasing the total distance light propagates in a tissue, permitting deep - tissue interrogation with sources and detectors placed on the surface.

Formally, DOS quantifies tissue optical properties in the form of absorption (μ_a), and reduced scattering coefficients, (μ_s'). Tissue absorption coefficient, μ_a, is defined such that $1/\mu_a$ is the average distance traveled by light in the tissue before it is absorbed. Thus, μ_a represents the probability for the photon to be absorbed per unit length traveled [6, 19]. In a similar way, tissue scattering coefficient, μ_s, represents the probability of photon scattered per unit distance traveled, *i.e.,* $1/\mu_s$ is average distance traveled by the photon before it's direction changes due to scattering. A related quantity is the tissue reduced scattering coefficient, μ_s', which accounts for both the scattering length as well as the direction. $1/\mu_s'$

www.manaraa.com

is the average distance traveled by the photon before its direction is randomized.

$$\mu_s' = \mu_s(1-g) \tag{2.1}$$

Eq. 2.1 gives the relation between tissue scattering and reduced scattering coefficients, where, g is the anisotropy factor that characterizes the distribution of scattering angles. $g = 0$ indicates isotropic scattering *i.e.,* all angles are equally probable. $g = 1$ and $g = -1$ denote fully forward/back scattering respectively. Note that tissue is mostly forward scattering with $g \approx 0.91$.

The goal of tissue optical spectroscopy is to quantitatively measure the concentrations of tissue chromophores (typically oxygenated and deoxygenated hemoglobin), and changes therein due to events such as functional activation. The absorption of light in tissue is determined by the concentrations, and absorption cross-sections of chromophores in the tissue.

$$\mu_a = 2.303 \sum_i (\epsilon_i(\lambda) C_i) \tag{2.2}$$

where $\epsilon_i(\lambda)$ $M^{-1}cm^{-1}$ is the molar extinction coefficient of the i^{th} chromophore at wavelength λ, and C_i is the concentration of the i^{th} chromophore in M. In the near infrared (NIR) wavelengths (650 nm $-$ 950 nm) absorption of light by human tissue is dominated by oxygenated hemoglobin (HbO), deoxygenated hemoglobin (HbR). Other tissue chromophores such as fats, lipids, melanin, and water also absorb light, albeit to a lesser extent. Fig. 2.1 shows the relative absorption of tissue chromophores such as oxygenated hemoglobin (HbO), deoxygenated hemoglobin (HbR), water and fat in the NIR region. In order to estimate the concentrations, C_{HbO} and C_{HbR}, tissue spectroscopy techniques estimate μ_a at at least two wavelengths. The concentrations of non hemoglobin moieties can be estimated by

www.manaraa.com

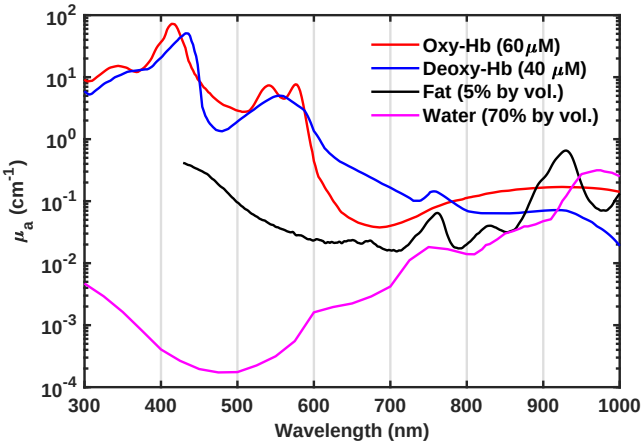

Figure 2.1: Optical properties of typical chromophores in tissue highlighting low absorption in the NIR spectral window ($700-900$ nm). Light in this part of the spectrum can penetrate several centimeters through skin and tissue, permitting deep-tissue measurements from optical measurements on the surface [18, 35, 36]

including measurements of μ_a from an additional wavelengths, with additional instrument cost and complexity. Alternatively, one could measure [6], or assume concentrations of non hemoglobin chromophores (that typically do not change during functional activation), and 'correct' experimentally measured values of μ_a. Indeed, it is common to assume a water volume fraction of 70% and incorporate the effect of water absorption in the Eq.2.2 as [3]

$$\mu_a^{corrected}(\lambda) = \mu_a^{measured} - \mu_a^{water} \tag{2.3}$$

Fig. 2.2 shows a classic setup for non invasive DOS measurement of *cerebral* hemodynamics. An optical fiber is used to direct light from a laser diode of wavelength in NIR region to a 'source position' on the surface of the scalp. The light propagates through the tissue and undergoes a series of absorption and scattering events; a fraction of the light that interacts with the tissue is reflected back to the tissue surface, where it is detected using another optical fiber at the 'detector position'. The shaded region depicts an approximation of the paths taken by photons as they travel from the source position to the detection position.

www.manaraa.com

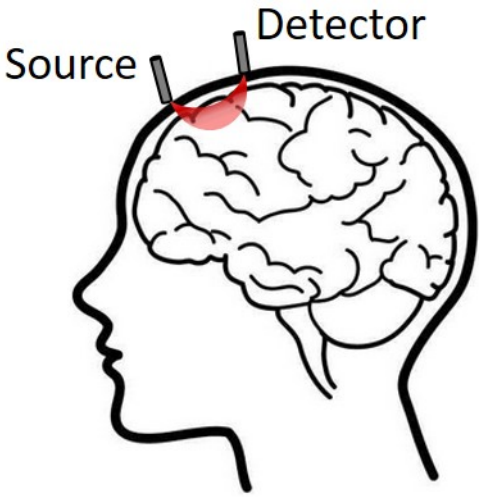

Figure 2.2: Example of the DOS measurement using a single source detector separation. Shaded region indicates most probable photon trajectories and thus a measure of the sampling volume of DOS measurements.

This diffusion of light through tissue, permits interrogation of tissue components/regions at depths ranging from millimeters to centimeters below the scalp. The detected light is attenuated by *both* absorption and scattering events occurring inside the tissue. Thus, we need a mathematical model of light transport to quantitatively measure the probability of interaction of photon due to absorptive and/or deflective behavior. Note however that tissue components such as blood primarily impact changes in the tissue absorption coefficient only (Eq. 2.2), and not scattering coefficients [6].

2.2 Photon Diffusion Equation

The propagation of light through a tissue can be modeled as a diffusion process and as such described using a Photon Diffusion Equation [9, 4, 19].

$$\nabla[D(\boldsymbol{r},t)\nabla\phi(\boldsymbol{r})] - v\mu_a(\boldsymbol{r},t)\phi(\boldsymbol{r},t) - \frac{\partial\phi(\boldsymbol{r},t)}{\partial t} = vS(\boldsymbol{r},t). \tag{2.4}$$

Here, $\phi(\boldsymbol{r},t)$ is the photon fluence rate at tissue position $\boldsymbol{r}$ in units of W/cm^2, $D(\boldsymbol{r})$ is the photon diffusion coefficient defined as $D = v/3(\mu_s'(\boldsymbol{r}) + \mu_a(\boldsymbol{r}))$ in units of cm^2/s,

www.manaraa.com

$\mu_a(\boldsymbol{r})$ and $\mu_s'(\boldsymbol{r})$ are the position dependent absorption and reduced scattering coefficients of the tissue in cm^{-1},and v is the speed of light in tissue in cm/s. $S(\boldsymbol{r},t)$ is the source term determining the amount of light illumination in tissue. If we assume that the optical properties are assumed to be uniformly distributed in tissue, *i.e.,* tissue is homogeneous, Eq. 2.4 can be simplified to

$$D\nabla^2\phi(\boldsymbol{r},t) - v\mu_a\phi(\boldsymbol{r},t) - \frac{\partial\phi(\boldsymbol{r},t)}{\partial t} = vS(\boldsymbol{r},t). \tag{2.5}$$

The photon diffusion equation is derived as an approximation from radiative transport theory [6], and it is important to note the conditions where it is appropriate to apply it to describe tissue light propagation [19]. Most importantly, diffusion theory is valid only in tissue that is dominated by scattering, *i.e.,* $\mu_s' > \mu_a$. For cerebral tissues $\mu_a \approx 0.1-0.2$ cm^{-1}, and $\mu_s' \approx 7-10$ cm^{-1}. Diffusion theory also assumes that the direction of light in tissue is randomized. This validity condition places a limit on the source-detector separations where diffusion can be applied. As a rule of thumb, the source-detector separation, ρ, should be greater than three times the tissue mean free path, *i.e.,* $\rho > \frac{3}{\mu_s'}$. Finally, we assume that the rate of temporal changes in fluence rate are slower than the speed of light.

2.2.1 Types of DOS Sources

Practical implementation of Diffuse Optical Spectroscopy, via solutions to Eq. 2.5 or Eq. 2.4, requires definition of the source term. For any implementation, we are required to use equal or more number of wavelengths than the number of chromophores. The three typical implementations of DOS are:

1. Continuous Wave Near Infrared Spectroscopy (CW-NIRS)
2. Frequency Domain Near Infrared Spectroscopy (FD-NIRS)

www.manaraa.com

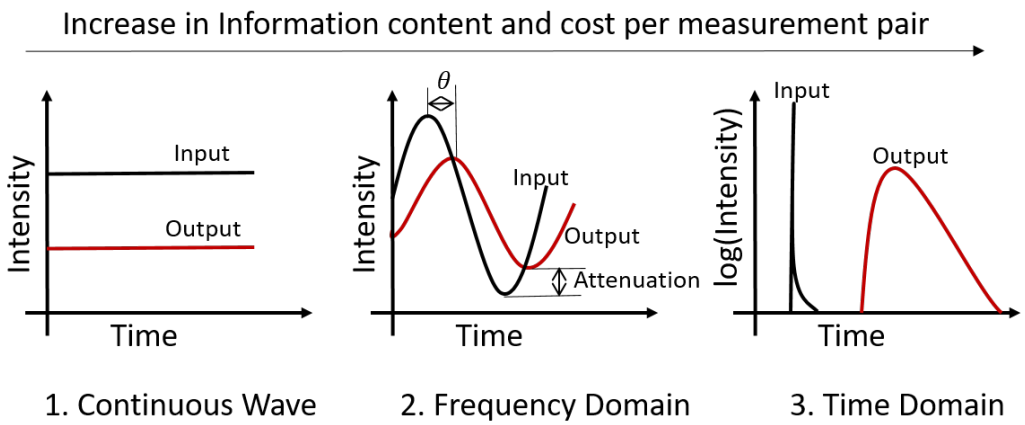

Figure 2.3: Three types of sources for DOS/NIRS measurement. 1. Continuous wave DOS or NIRS, where tissue is illuminated with a source of light at constant intensity. The changes in the detected intensity are used to compute the changes in the absorption and scattering properties of the tissue.2. Frequency Domain DOS, where tissue is illuminated with light sources whose intensity is modulated at a specific (RF) frequency. The changes in the phase shift and attenuation of the detected intensity (w.r.t source) are used to compute the absolute values of tissue optical properties. 3. Time domain DOS, where tissue is illuminated with a pulsed (femto or pico-second) light source. The photon arrival times of the detected light are used to compute the absolute tissue optical properties. Adapted from [19].

3. Time domain Near Infrared Spectroscopy (TD-NIRS)

Time domain (or time-resolved) measurements, involve use of multiple near infrared light sources to launch short light pulses into the tissue and measure the time of flight of the detected photons from the tissue. Tissue acts as a low pass filter, which has the effect of broadening the input pulses; the shape of the broadened pulse can be fit to a time-resolved solution to Eq. 2.5 to compute tissue optical properties, from measurements are only one source-detector separation [3, 41, 32] . Although this method provides an avenue to calculate the absolute properties, the complexity of instrumentation and the cost involved, make time domain methods practically difficult to implement. Time domain NIRS is not used in this thesis and is included here for only completeness.

A simpler, and comparatively less expensive alternative is Frequency Domain Near Infrared Spectroscopy, where tissue is illuminated with intensity modulated light. Measure-

www.manaraa.com

ments of the amplitude and phase changes at multiple source-detector separations (w.r.t the source modulation) are used to compute tissue optical properties. Note that the frequency domain and time domain methods are related via the Fourier transform. The frequency domain method is described in greater detail in Sec 2.4. The final, and simplest, implementation of DOS is Continuous Wave NIRS. Continuous wave DOS can be thought of as a limiting case of the frequency domain approach with modulation frequency set to zero. Here, tissue is illuminated by light of constant intensity from multiple wavelengths. CW NIRS is described in greater detail in Sec 2.3. The motive of this thesis is utilization of Continuous Wave and Frequency Domain measurements for the measurement of optical properties in functional activation measurements. These two techniques are briefly explained in the following two sections.

2.3 Continuous Wave DOS or Near Infrared Spectroscopy (NIRS)

Continuous Wave Diffuse Optical Spectroscopy, typically referred to as Near Infrared Spectroscopy (NIRS), is the simplest implementation of tissue spectroscopy. CW-NIRS utilize light sources which emit light at a constant amplitude to illuminate the tissue. In this modality, the DC component of the attenuated light is collected at the detector. Solving Eq. 2.5 for continuous wave source in a homogeneous semi-infinite media we have

$$\phi_{cw} = \frac{vS_0}{4\pi D\rho} \exp\left(-\sqrt{\frac{v\mu_a}{D}}\rho\right) \tag{2.6}$$

It is difficult, almost impossible, to quantitatively determine/separate the optical properties from CW-NIRS measurements even with multiple source detector separations [2]. In particular, we cannot separate the attenuation effects of absorption from scattering. Thus, to measure μ_a from the CW measurement, values of the tissue scattering coefficients μ_s' are

www.manaraa.com

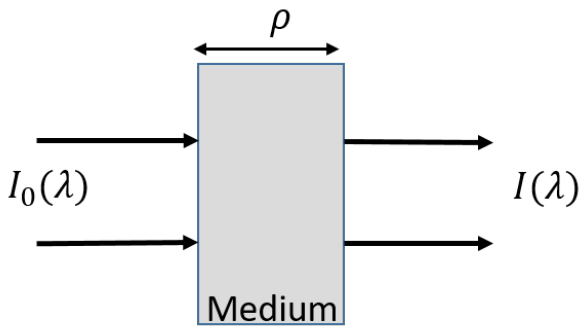

Figure 2.4: The propagation of light in a non scattering or homogeneous medium slab of thickness ρ. $I_0(\lambda)$ is the intensity of light incident on the medium and $I(\lambda$ is the attenuated light intensity after being absorbed by medium

typically assumed. As a result, to appropriately account for tissue scattering effects and solve for changes in tissue absorption, we use of an alternative and a simple approach to solve the CW measurement, known as the Modified Beer-Lambert law. Using this method, researchers [24, 43, 23] were able to measure the temporal hemodynamic changes due to auditory stimulations at even a single distance CW measurement. The attenuation of light (or other electromagnetic radiation) through non-scattering homogeneous media is described by the Beer-Lambert law.

$$I(\lambda) = I_0(\lambda) \exp\left(-\mu_a(\lambda)\rho\right) \tag{2.7}$$

where I_0 is the intensity of the light source, I is the intensity of light measured after it has traveled a distance ρ through homogeneous media. Beer Lambert law holds true for non scattering media ($\mu_s' = 0$), and for dilute solutions (Fig.2.4).

www.manaraa.com

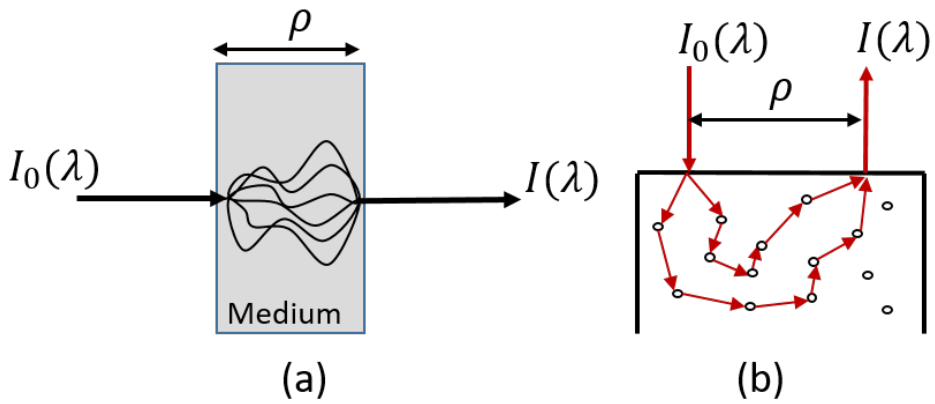

Figure 2.5: Representation of the propagation of light in a scattering medium.(a) The propagation of light in a scattering or dilute medium slab of thickness ρ- transmission geometry. (b) The different paths of propagation of light through a semi infinite homogeneous tissue with scattering taking place at each collision.

The Beer Lambert law in Equation 2.7 can be rewritten in the form of molar extinction coefficients ($\epsilon(\lambda)$) and concentration of the chromophores (C) in the media.

$$\begin{aligned} OD &= -\log\left(\frac{I(\lambda)}{I_0(\lambda)}\right) \\ &= \mu_a(\lambda)\rho \\ &= \Sigma_i(\epsilon_i(\lambda)C_i)\rho \end{aligned} \tag{2.8}$$

In a scattering medium, attenuation of light occurs both due to absorption (energy is absorbed by the medium *along* the light path) and scattering (energy is scattered *away* from the light path). Thus, Eq. 2.8 cannot be applied directly to measure tissue absorption. To account for scattering, we use the modified Beer-Lambert law (MBL) which is an extension of the Beer-Lambert law to turbid media with high absorption and scattering properties. Briefly, the modified Beer-Lambert law employs a new parameter *Differential Path length Factor (DPF)*, in order to account for the change in path of the light due to scattering in tissue. The Modified Beer-Lambert law relates the *change* in optical density to the *change*

www.manaraa.com

in tissue absorption

$$\Delta OD(\lambda) = -\log\left(\frac{I(\rho)}{I_0(\rho)}\right)$$
$$\simeq \Delta\mu_a(\lambda) DPF(\lambda) \tag{2.9}$$

where, $\Delta OD(\lambda)$ is the change in optical density, $DPF(\lambda)$ is the differential path length factor, rho is the source detector separation, and $\Delta\mu_a(\lambda)$ is the change in tissue absorption coefficient.

In contrast to the Beer-Lambert law (Eq.2.7), where we measure the absolute absorption coefficient, with Modified Beer-Lambert law (Eq.2.9) we measure the *changes* in the absorption co-efficients [30, 14]. Using the Modified Beer Lambert law we measure the differential optical density and convert these changes in the intensity to the relative changes in the concentration of tissue chromophores. This is represented by the simplified equation in Eq. 2.10

$$\Delta OD(\lambda) = \Sigma_i\big(\epsilon_i(\lambda)\Delta C_i(\lambda) DPF(\lambda)\rho\big) \tag{2.10}$$

where $\epsilon_i(\lambda)$, $C_i(\lambda)$ are molar extinction co-efficients and concentration of the i^{th} chromophore at wavelength λ respectively. The *Differential Pathlength Factor* can be calculated based of assumed baseline tissue optical properties [6], experimentally measured with pulsed-time techniques [35], or with Monte-Carlo simulations [25, 30]. For the auditory functional activation measurements in this thesis, we assumed DPF to be 5.86 and 6.51 for measurements at wavelengths 830 nm and 690 nm respectively [17]. As DPF is a ratio, it is a dimensionless quantity. It must be noted that one of the drawbacks of the CW- NIRS system is its inability to measure the absolute absorption and scattering coefficients as it can only measure the relative changes. Nonetheless, CW-NIRS is still the most commonly used technique to study

www.manaraa.com

functional activation [27, 11, 24] as it is economical and has simple instrumentation. Some of commercial CW-NIRS systems include CW-6 (Techen Inc.), ETG-4000 (Hitachi Medical co.) and NIRScout (NIRx Medical Technologies LLC).

2.4 Frequency Domain Diffuse Optical Spectroscopy

Frequency Domain Diffuse Optical Spectroscopy(FD-DOS) instruments utilize NIR light sources whose intensity is sinusoidally modulated in the range of $\sim$ 100 MHz or more [1, 7, 40]. This sets up a diffusive photon density wave (DPDW) in the tissue at the modulation frequency, the wave-vector of which (characterized from the phase shift and amplitude of the detected light) is used to estimate tissue optical properties. In general, FD-DOS systems are more complex and expensive than the CW system, but the additional information obtained therein makes it a worthy trade-off. Furthermore, since FD systems measure light only at the modulation frequency, they tend to be less sensitive to the stray room light. However, since FD-DOS measurements are dependent on the absolute values of measured intensity, they can be more sensitive to the light leakage from the sources and to the optical fiber coupling with tissue. This latter issue is often solved by a calibration process which is explained in detail in Sec. 3.3.1.

Conventionally, FD-DOS systems utilize two phase-sensitive demodulation techniques [6, 31, 17]. The first, homodyne detection, mixes the detected light (signal) with the in-phase and phase-shifted RF modulation frequency of source (reference), to measure the in-phase and quadrature components of the detected light (with reference to the source) respectively. Thus the phase, and amplitude of the DPDW is estimated with RF electronics. The second approach, heterodyne detection, converts the detected signal to a lower frequency (in KHz),

www.manaraa.com

by mixing the detected light (signal) with a frequency shifted reference. Lock-in techniques are then used to estimate the phase and amplitude of the DPDW. The device used in this thesis utilizes heterodyne demodulation with a cross correlation or 'beat' frequency of ~ 5 KHz. Finally, amplitude and phase of the DPDW is conventionally measured at multiple distinct source-detector separations; amplitude decreases exponentially with distance, and phase increases linearly with distance [6, 31, 10, 21].

We now briefly review the mathematical underpinnings behind FD-DOS. The differential equation for the Diffuse Photon Density Wave (DPDW) can be derived from the Photon diffusion equation (Eq.2.4), by substituting for a sinusoidally modulating source term, *i.e.*, $S(\boldsymbol{r},t) = S_{dc} + S_{ac}\exp(-i\omega t)$. The resulting DPDW equation for homogeneous medium is given by [6, 7, 40]

$$\left(\nabla^2 - \kappa^2\right)\phi(\boldsymbol{r}) = -\frac{v}{D}S_{ac}. \tag{2.11}$$

where, κ is the complex wave-vector of the DPDW defined by $\kappa^2 = (v\mu_a - i\omega)/D$, ω is the source modulation frequency, and S_{ac} is the amplitude of the source modulation. As before, μ_a and D are the tissue absorption and photon diffusion coefficients respectively, and $\phi(\boldsymbol{r})$ is the fluence rate of light at position $\boldsymbol{r}$ in tissue. The solution to Eq. 2.11, for a homogeneous semi-infinite geometry and an extrapolated zero boundary condition [6, 19], can be derived using a Greens' function approach. The measured fluence rate $\phi_{FD}(\rho, z=0)$, at the tissue surface $z=0$ and a source-detector separation of (ρ) is given by

$$\phi_{FD}(\rho, z=0) = \frac{vS_0}{4\pi D}\left(\frac{\exp(-\kappa r_1)}{r_1} - \frac{\exp(-\kappa r_b)}{r_b}\right)_{z=0} \tag{2.12}$$

where $r_1 = \sqrt{\rho^2 + (z - l_{tr})^2)}$, $r_b = \sqrt[2]{\rho^2 + (z + l_{tr} + 2z_b)^2)}$ are the origination points of two spherical waves (source and image) that combine to provide zero fluence rate at the

www.manaraa.com

extrapolated zero boundary $z_b = 2(1+R_{eff})/3\mu_s'(1-R_{eff})$, $\phi(\rho, z_b) = 0$. R_{eff} is the amount effective reflection coefficient of the tissue-air boundary, $l_{tr} \approx 1/\mu_s'$ is the photon mean free path, and S_0 is the amplitude of the source fluence. When considering source-detector separation much larger than the mean free photon transport path, *i.e.*, $\rho \gg l_{tr}$, Eq. 2.12 simplifies to

$$\begin{aligned}\phi_{FD}(\rho) &\approx \frac{vS_0}{4\pi D}\frac{e^{i\kappa\rho}}{\rho^2}[-2i\kappa(l_{tr}z_b + z_b^2)] \\ &= A(\rho)e^{i\theta(\rho)}\end{aligned} \tag{2.13}$$

Here $\theta(\rho)$ and $A(\rho)$ are the phase and amplitude of the light detected from the tissue. Eq. 2.13 can further be linearized to arrive at [19]

$$\log\left(A(\rho)\rho^2\right) = -\kappa_i\rho + A_0, \tag{2.14}$$

and

$$\theta(\rho) = \kappa_r\rho + \theta_0 \tag{2.15}$$

where, κ_r and κ_i are the real and imaginary parts of the complex DPDW wave vector κ. From Eq. 2.14 and Eq. 2.15, it is readily apparent that the amplitude exponentially decreases with source detector separation, and phase linearly increases with source detector separation. Fig. 2.6 shows the plot of amplitude and phase versus the source detector separation.

Thus, measurements of DPDW amplitude and phase at multiple source detector separations permit the estimation of the slopes κ_i and κ_r. Indeed, it is straightforward to show that κ_i and κ_r are directly related to the tissue optical properties.

$$\kappa_r = \left(\frac{\mu_a v}{2D}\left(\sqrt{1+\left(\frac{w}{v\mu_a}\right)^2}+1\right)\right)^{1/2} \tag{2.16}$$

www.manaraa.com

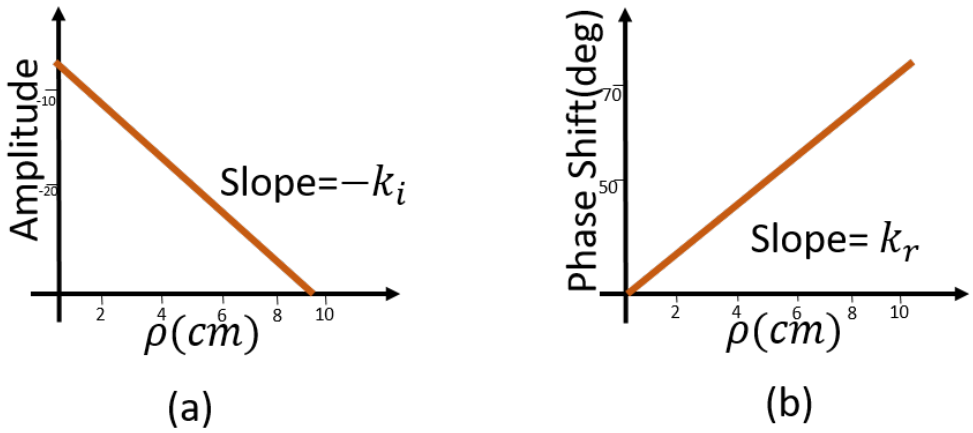

Figure 2.6: Relationship between amplitude and phase with source detector separation ρ. (a) $\log(A(\rho)\rho^2)$ versus source detector separation ρ with slope $-\kappa_i$. (b) Phase $\theta(\rho)$ versus the source detector separation ρ with slope κ_r.

$$\kappa_i = \left(\frac{\mu_a v}{2D} \left(\sqrt{1 + \left(\frac{w}{v\mu_a} \right)^2} - 1 \right) \right)^{1/2} \tag{2.17}$$

From Eqs. 2.16 and 2.17, it is straight-forward to estimate μ_a and μ_s' from the slopes κ_r and κ_i

$$\mu_a = \frac{\omega}{2v} \left(\frac{\kappa_i}{\kappa_r} - \frac{\kappa_r}{\kappa_i} \right) \tag{2.18}$$

$$\begin{aligned} \mu_s' &= \frac{2v}{3\omega} \kappa_i \kappa_r - \mu_a \\ &\approx \frac{2v}{3\omega} \kappa_i \kappa_r \end{aligned} \tag{2.19}$$

Finally, the concentrations of the tissue chromophores are estimated from μ_a estimated at different wavelengths, as previously described in Sec. 2.1

www.manaraa.com

CHAPTER 3: INSTRUMENTATION AND METHODS

3.1 Frequency Domain Diffuse Optical Spectroscopy Instrument

A commercial Frequency-Domain Diffuse Optical Spectroscopy instrument, Imagent (ISS, Inc., IL, USA), was used in this study to measure functional activation from the auditory cortex. Briefly, the Imagent system utilized for this study consists of 64 light sources (laser diodes) split evenly between two wavelengths 690 nm and 830 nm. Imagent utilizes a time multiplexing scheme to differentiate optical signals from each source. Thus, with 32 laser diodes for each wavelength, the instrument can be implemented to illuminate up to 32 independent source positions. The average power of the laser diodes is ~ 10 mW, which is less than the ANSI limits of light-skin illumination [44].

The light sources are modulated at a frequency of 110 MHz. Thus, the output light intensity of the laser diodes can be modeled as $I(t) = I_0^{DC} + I_0^{AC} \sin(2\pi f t - \phi_0)$, where $I(t)$ is the intensity modulated intensity of the source (mW/cm^2), f is the source modulation frequency (i.e., 110 MHz, ϕ_0 is the initial phase of source intensity modulation, I_0^{DC} and I_0^{AC} are the average and alternating component of the light source intensity respectively. Imagent also consists of 8 detectors (photomultiplier tubes, labeled A through H), with individually controllable gains. Light detected by the photomultiplier tubes is amplified, and the amplitude and phase of the detected light intensity (with reference to the source modulation) is measured via analog heterodyne demodulation [6, 26, 20]. Imagent uses a

www.manaraa.com

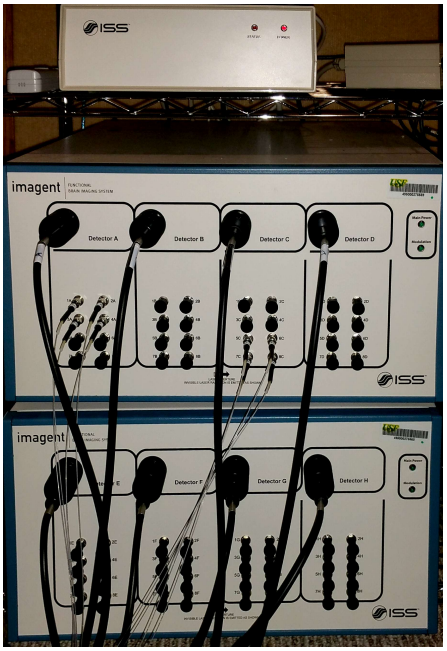

Figure 3.1: ISS Imagent, a commercial frequency domain-Diffuse Optical Spectroscopy instrument.

'beat' or 'cross-correlation' frequency of 5 KHz. Illumination of tissue, and detection of diffusely reflected light from tissue is accomplished via inert optical fibers. Specifically, multi-mode step-index fibers with a core diameter of 400 μm were used for illumination, while detection was realized by multi-mode fiber optic bundle with a total core diameter of 3 mm. Acquisition of amplitude and phase at each detector is implemented with a built-in USB data acquisition unit, and software (BOXY).

3.1.1 Instrument and Fiber Optic Setup

The current study utilized 8 laser diodes (4 each at 830 nm and 690 nm), arranged to illuminate the tissue at 4 source positions. Light reflected from the tissue was detected at 8 detector positions using the 8 photomultiplier tubes on the Imagent. The data acquisition software was setup to record data from all detectors in parallel, with the source laser diodes time-multiplexed to switch 'ON' in sequence, which permitted a sampling rate of $\sim$ 10 Hz (data collection rate). A custom probe (manifold) was 3D printed (Protolabs Inc.) to hold

www.manaraa.com

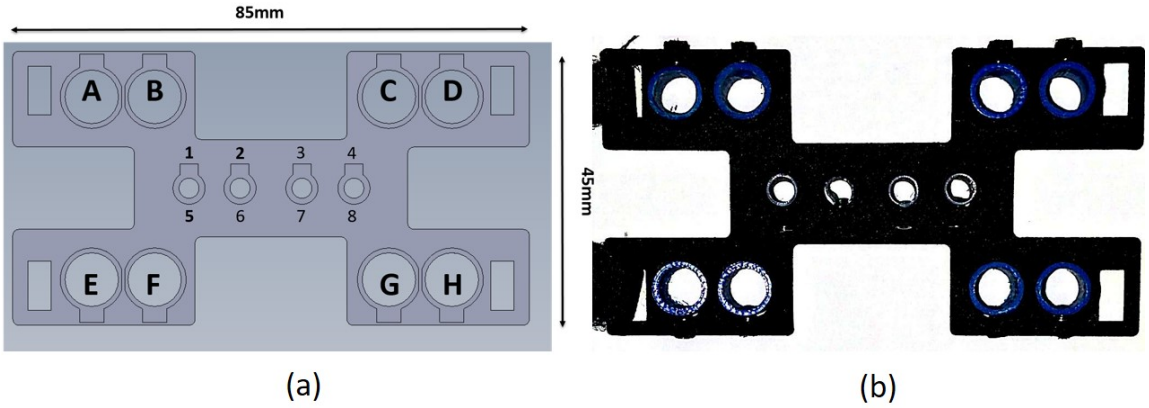

Figure 3.2: (a) A schematic diagram of manifold that functioned as a custom fiber optic probe. It has 8 detectors (A through H) and four overlapping source positions for $\lambda = 690$ nm (1 through 4), and for $\lambda = 830$ nm (5 though 8). (b). The 3D-printed manifold (Protolabs Inc.) used.

the source and detector fibers at their desired separations.The arrangement of source fibers and detector fibers on the probe is shown in Fig. 3.2. Note that physical positions of sources 1 through 4 ($\lambda = 690$ nm), and 5 though 8 ($\lambda = 830$ nm) overlap on the probe. This arrangement is practically realized via a custom bifurcating fiber, with the distal ends connected to the respective laser diodes on the Imagent and the proximal end connected to the desired source position on the probe. Tab. 3.1 highlights the distances between the each source and detector position used in the custom fiber optic probe.

www.manaraa.com

Table 3.1: Source-detector separations realized by the custom fiber optic probe. The schematic of the probe is shown in Fig. 3.2. All distances are in cm.

Sources / Detectors	1 and 5	2 and 6	3 and 7	4 and 8
A	2.183	2.866	3.772	4.554
B	1.610	2.081	2.882	3.625
C	3.638	2.880	2.076	1.616
D	4.568	3.769	2.864	2.193
E	2.183	1.610	3.638	4.568
F	1.610	2.081	2.882	3.625
G	3.638	2.880	2.076	1.616
H	4.568	3.769	2.864	2.193

The average source-detector separation is $\sim$ 3 cm, which is in line with prior fNIRS studies on functional activation of the auditory cortex [24, 27, 11]. The outputs obtained from the system , viz., modulation (AC), average (DC) and phase (ϕ) for each source detector separation, was stored in the computer for post-processing (Sec. 3.2 and 3.3).

3.1.2 Subjects

Nine healthy adults with normal hearing participated in this study: six females (aged 20$\pm$30 years) and three males (aged 25$\pm$35 years). All participants were informed about the

www.manaraa.com

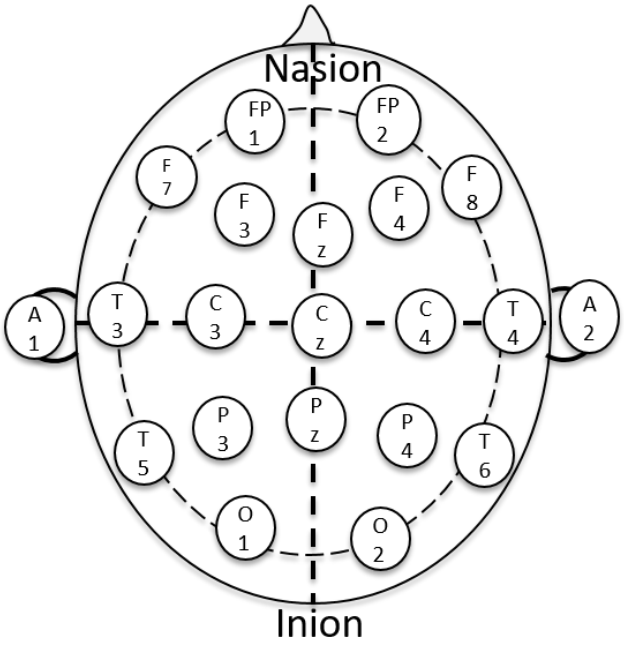

Figure 3.3: The International 10-20 system describing the location scalp electrodes.

experimental details/protocols and completed an approved informed consent form per the Institutional Review Board at the University of South Florida. All the subjects were tested for normal hearing via an auditory screening process including a hearing test, a tone test and a pressure test. Optical measurements were performed over the right auditory cortex.

3.1.3 Experiment Protocol

All experimental protocols, auditory stimuli and instruments were approved by the Institutional Review Board($CR5\_Pro00011325$) of the University of South Florida. The Imagent fNIRS system was warmed up for ~ 10 min prior to the measurement, and testing was conducted in a sound proof booth with dimmed lights to avoid interference of eternal lights and sounds. Subjects were seated comfortably on a reclining chair, with the fiber-optic probe affixed to their head above the auditory cortex.

www.manaraa.com

Figure 3.4: Placement of the probe on the T4 location above the Tragus on subject during an experiment

More specifically, the international $10-20$ system was used to guide probe placement over the auditory cortex [29]. It is generally understood that the auditory activation area in the human cerebral cortex is above the Tragus and around the T4 region [27, 43, 24, 11]. Here, we placed the probe on the head such that the sources lie on either side of T4 position. For accurate localization of the T4 position on a subjects head, the diameter of the head, the distances from Inion to Nasion and from right Tragus to the left Tragus were measured. The T4 position was identified to be 10% of the distance between right Tragus to the left Tragus towards the center of the head (see Fig. 3.3). The probe was fixed in position using the velcro straps, as shown in Fig. 3.4. By positioning the center of the sources (and the probe) over the T4 position, and having detectors on either side of the sources, we are well placed to be sensitive to hemodynamic changes over the entire auditory cortex. In particular, we expect a higher response in the regions of detectors A, B, E, and F [43, 37, 23, 11, 24].

After the probe has been positioned on the subject, two different auditory stimuli, a 1000 Hz pure-tone and Broadband noise, were presented bilaterally via insert ear phones

www.manaraa.com

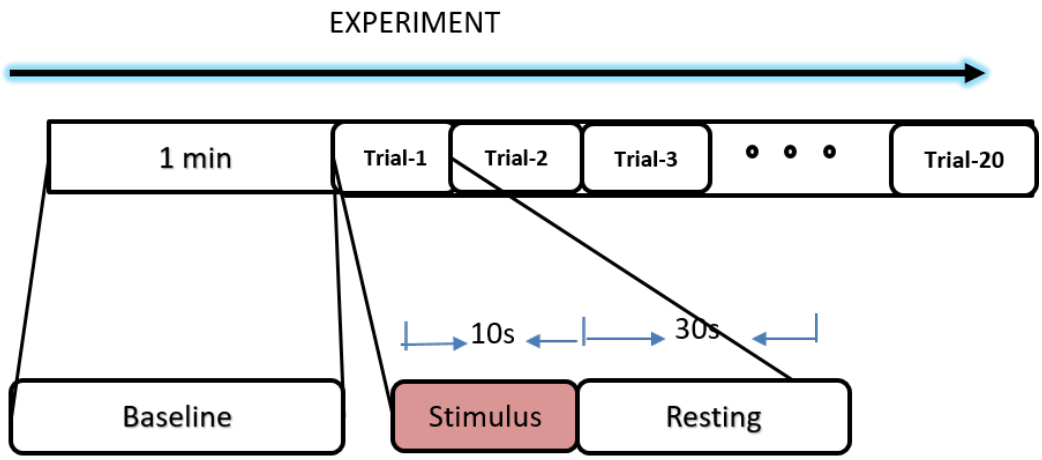

Figure 3.5: The protocol used for the functional activation experiment. A 1 min of baseline measurement, followed by 20 presentations of the 10sec stimuli and 30 sec resting period. The duration one experiment consisting of 20 trials lasted for 14 min.

(ER-2, Etymotics Inc., FL). The auditory stimuli were generated using *SigGen* through a TDT-RP2 (Tucker Davis Technologies, Alachua, FL) signal processor at 70 db sound pressure level (SPL). Each stimuli was presented 21 times (10 s stimulus followed by rest period of 30 s). Fig. 3.5 shows an outline of the experimental protocol. The entire experiment for one stimuli took about 14 min, including a 60 s baseline prior to stimuli presentation. Throughout, average light intensity (dc), amplitude (ac) and phase (ϕ) were continuously recorded, along with a marker of the stimulus presentation. Amplitude and phase data were analyzed with custom MATLAB scripts (Mathworks Inc., Natick, MA), using both the modified Beer-Lambert approach (Sec. 3.2), and the multi-distance FD-DOS method (Sec. 3.3), to compute the hemodynamic changes due to auditory stimulation.

3.2 Measurement of Optical Properties Using Modified Beer-Lambert Analysis

The light intensities (ac) measured for each source-detector separation (Tab. 3.1) was used to compute the *change* in concentrations of oxygenated and deoxygenated hemoglobin due to functional activation. Fig. 3.6 describes the step by step process for the Modified Beer-

www.manaraa.com

Lambert analysis of the recorded data, based on the theories described previously (Sec. 2.3). All processing steps were implemented in MATLAB (Mathworks, Natick, MA). Briefly, the average intensity data for each detector (and each source-detector separation) were first low pass filtered (cut off frequency of 0.1 Hz [24]) to remove pulsatile signals due to the heart rate and respiration.

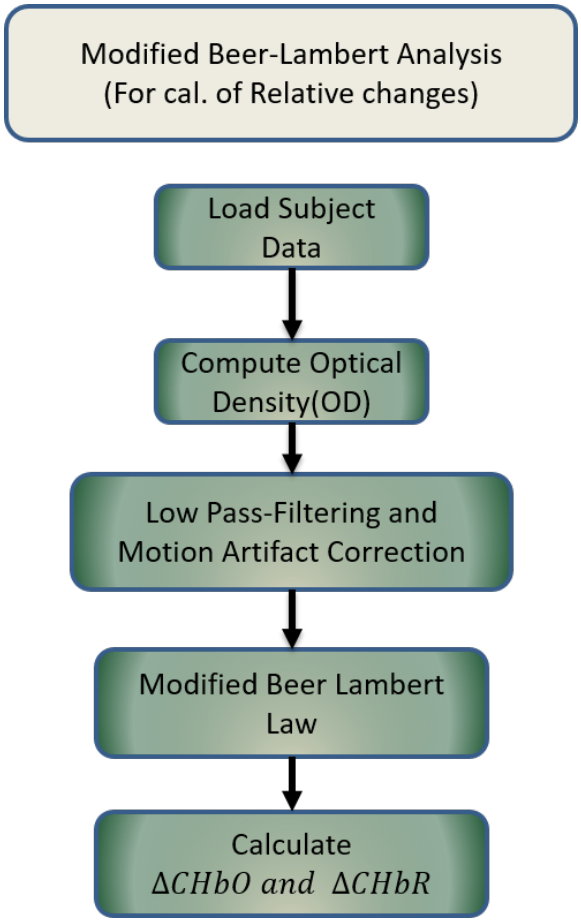

Figure 3.6: The process flow in a Modified Beer-Lambert approach for the measurement of concentration.

The filtered and motion artifact-corrected data is then analyzed using the Modified Beer-Lambert law (Sec. 3.2), to estimate changes in concentrations of the oxygenated and deoxygenated hemoglobin. For the two wavelengths being used in our case, Eq. 2.10 can be

www.manaraa.com

rewritten in matrix format for ease of computation.

$$\begin{bmatrix} \Delta OD(\lambda_1) \\ \Delta OD(\lambda_2) \end{bmatrix} = \begin{bmatrix} \epsilon_{HbO}(\lambda_1) DPF(\lambda_1) d & \epsilon_{HbR}(\lambda_1) DPF(\lambda_1) d \\ \epsilon_{HbO}(\lambda_2) DPF(\lambda_2) d & \epsilon_{HbR}(\lambda_2) DPF(\lambda_2) d \end{bmatrix} \cdot \begin{bmatrix} \Delta C_{HbO} \\ \Delta C_{HbR} \end{bmatrix} \tag{3.1}$$

Eq. 3.1 can be readily inverted to compute ΔC_{HbO} and ΔC_{HbR} in mol/ l. Here, $\lambda_1 =$ 690 nm, $\lambda_2 = 830$ nm, d is the source-detector separation of the measurement in cm, and $DPF(\lambda_i)$ is the differential path length factor for wavelength λ_i. $\epsilon_{HbO/R}(\lambda_i)$ is the molar extinction coefficient of the HbO/HbR at wavelength λ_i in $\text{cm}^{-1}/$ mol [36]. Changes in optical density (ΔOD) in Eq. 3.1 were calculated on a trial-by-trial basis, with the average measured intensity 5 s before the auditory stimulus being used as baseline. Prior to application of the modified Beer-Lambert law, OD time courses were processed to remove motion artifacts[8]. A moving standard deviation filter (n = 4) was first applied to the OD data to calculate the local variance; motion artifacts were then identified as regions in the signal with high local standard deviation (threshold $\gg 2.0$). Trials with significant motion artifacts were excluded from the analysis. Changes in C_{HbO} and C_{HbR} were then computed with $DPF(690 \text{ nm}) =$ 5.86 and $DPF(830 \text{ nm}) = 6.51$ [17]. Finally, stimulus induced changes ΔC_{HbO} and ΔC_{HbR} from all presented trials were averaged to arrive at the results for each subject. Note that the modified Beer-Lambert analysis estimates hemodynamic changes for each source-detector separation, *i.e.,* 4 curves for each detector.

3.3 Measurement of Optical Properties Using Photon Diffusion Equation

The amplitude (ac) and phase (ϕ) of light intensities measured at each detector as a function of source-detector separation (Tab. 3.1) was used to compute the *absolute* concentrations of oxygenated and deoxygenated hemoglobin due to functional activation. The data analysis process is summarized in Fig. 3.7, based on the multi-distance FD DOS meth-

www.manaraa.com

ods described in Sec. 2.4. All processing steps were implemented in MATLAB (Mathworks, Natick, MA).

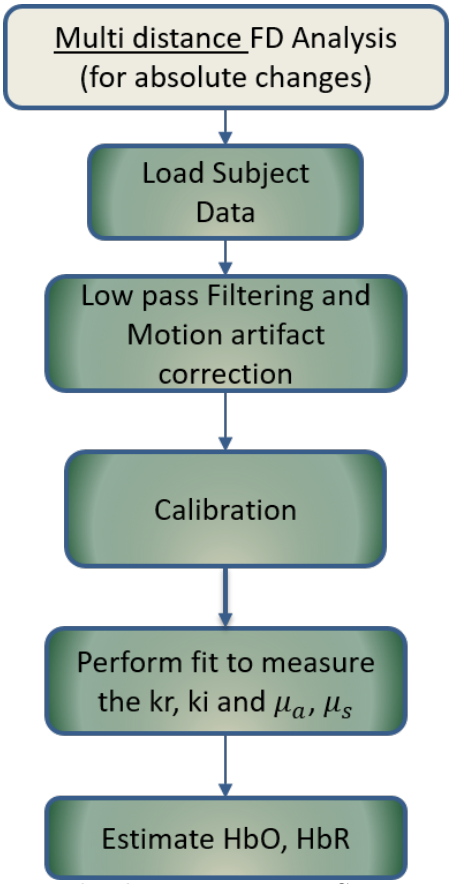

Figure 3.7: The process flow in a multi-distance FD-NIRS approach for the measurement of concentration.

Amplitude and phase data were pre-processed (low pass filter, motion artifact correction) using methods similar to those described in Sec. 3.2. The pre-processed amplitude and phase measurements at each wavelength were ordered as a function of source-detector separation for each detector. Recall from section 2.4, that optical properties of the tissue under study (*i.e.*, μ_a and μ_s) are related to the slopes κ_r and κ_i of amplitude and phase as a function of source-detector separation (ρ). For accurate recovery of tissue optical properties, it is important to perform a calibration procedure (described in detail in Sec. 3.3.1) of ampli-

www.manaraa.com

tude and phase data. Phantom calibration was performed at the beginning of each subject measurement, and the calibration coefficients obtained therein were applied to the data collected from that subject to account for differential tissue-fiber coupling. Once calibrated, κ_r and κ_i were estimated by performing a linear fit of $log(\rho^2 A(\rho))$ and ϕ as a function of source-detector separation (ρ), as per Eqs. 2.14 and 2.15 in Sec. 2.4. Thes estimates were then used with Eqs. 2.18 and 2.19 to calculate the tissue optical properties μ_a and μ_s at both wavelengths.

Background absorption (due to water) was corrected using Eq. 2.3 before computing time series of C_{HbO} and C_{HbR} over the experiment duration (Eq. 2.2). Finally, as in Sec. 3.2, stimulus induced changes in hemoglobin concentrations, ΔC_{HbO} and ΔC_{HbR} from all presented trials were averaged to arrive at the results for each subject. Note that unlike with the modified Beer-Lambert analysis, the multi-distance photon diffusion approach estimates 1 pair of hemodynamic curves for four source-detector separations.

3.3.1 Calibration

Estimation of optical properties with FD-DOS requires measurement of real and imaginary parts of the DPDW wave vector, from measurements of amplitude and phase at different

Table 3.2: Optical properties of ISS phantom in cm^{-1}

Wavelength	μ_a	μ_s'
830 nm	0.154	4.4
690 nm	0.158	5.2

www.manaraa.com

source-detector separations. In Sec. 2.4, we described the relations Eq. 2.14 and Eq. 2.15 for amplitude and phase of the detected light intensity with respect to the source intensity modulation [1]. These equations are used for estimating the two unknowns quantities, *i.e,* the tissue absorption (μ_a) and reduced scattering coefficient (μ_s'). Practically, two additional unknowns account for the variations in the light coupling between the tissue surface and the source and/or detector. In order for this procedure to yield accurate tissue optical properties, it is important to maintain constant/consistent light coupling efficiencies at each fiber-tissue interface. Since this is hard to achieve experimentally, it is common to perform a calibration procedure using a tissue simulating phantom of known optical properties [9, 3]. For the calibration process, we used two tissue simulating phantoms with known optical properties (μ_a) and (μ_s'). The first calibration phantom used was manufactured by ISS Inc. and the second phantom used was manufactured by the INO Inc. (Biomimic, Institut National d'Optique). The optical properties of these phantoms are given in Tabs. 3.2 and 3.3.

Table 3.3: Optical properties of Biomimic phantom in cm^{-1}

Wavelength	μ_a	μ_s'
830 nm	2.183	2.866
690 nm	1.610	2.081

Briefly, we compare the measured amplitude and phase as a function of source-detector separation from the tissue phantom, to the values expected from a homogeneous semi-infinite FD-DOS solution (Eq. 2.14 and 2.15) for the phantom optical properties. The effect of the coupling coefficients occurring in a phantom measurement on the measured intensity can be

www.manaraa.com

written as [3]:

$$I_{ij} = I_{ij}^{PM} \exp(-i\phi_{ij}^{PM})$$
$$= C_A I^{PT}(\rho_{ij}) \exp\left(-iC_{c,P}\theta^{PT}(\rho_{ij})\right) \tag{3.2}$$

where I_{ij}^{PM} and ϕ_{ij}^{PM} are the measured intensity and phase on the phantom for i^{th} source and j^{th} detector respectively with a source detector separation of ρ. $I^{PT}(\rho_{ij})$,$\theta^{PT}(\rho ij)$ in turn are the amplitude and phase expected from a homogeneous semi-infinite solution to the photon diffusion equation for the given phantom optical properties. C_A , C_ϕ are the terms accounting for the effect of coupling coefficients of i^{th} source and j^{th} detector on measured amplitude $|I_{ij}^{PM}|$ and measured phase ϕ_{ij}^{PM} respectively. Thus, the amplitude and phase coupling coefficients can be written as:

$$C_{c,I} = \frac{|I_{ij}^{PM}|}{I^{PT}(\rho_{ij})} \tag{3.3}$$

$$C_{c,\phi} = \theta^{PM}(\rho_{ij}) - \theta^{PT}(\rho_{ij}) \tag{3.4}$$

Assuming that the light coupling coefficients present in the tissue measurement are same for the phantom, the measured amplitude $|I_{ij}^{TM}(\rho_{ij})|$ and phase $\theta^{TM}(\rho_{ij})$ obtained from the tissue can be appropriately corrected using the estimated calibration coefficients

$$|I_{ij}^{TM}(\rho_{ij})| = C_{c,I}|I^{TT}(\rho_{ij})| \tag{3.5}$$

$$\theta^{TM}(\rho_{ij}) = C_{c,\phi} + \theta^{TT}(\rho ij) \tag{3.6}$$

where $|I_{ij}^{TT}(\rho_{ij}|$ and $\theta^{TT}(\rho_{ij})$ are the corrected calculated amplitude and phase for tissue measurements.

Now the optical properties of the tissue can be retrieved from the corrected amplitude and phase by fitting these values to the values obtained from the photon diffusion model for all

www.manaraa.com

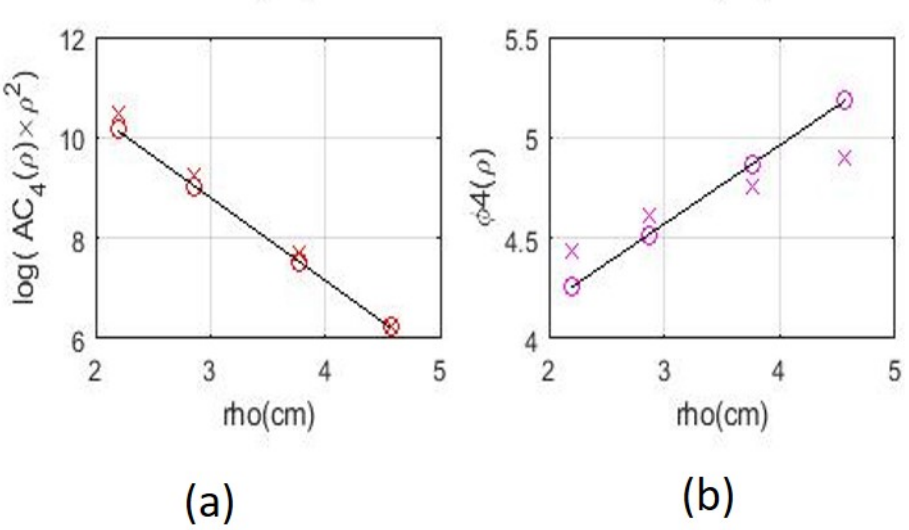

Figure 3.8: A representative graph for before and after calibration values of $\log(\rho^2 A(\rho))$ and Phase. (a) $\log(\rho^2 A(\rho))$ versus source detector separation ρ for detector 4. (b) Phase $\phi(\rho)$ versus the source detector separation rho. The crosses are the values of the measured amplitude. The circles represent the values after applying calibration. The slopes of the lines joining the calibrated values give κ_r and κ_i.

separations between sources and detectors. A representative figure showing this calibration by fitting is shown in Fig. 3.8. An advantage of using the above approach for calibrating the FD DOS measurements is the ability to use a diverse range of source detector separations. An important caveat however is the assumption that coupling coefficients for both tissue and tissue simulating phantom are similar. Of course, this assumption may be invalidated in the presence of the hair follicles underneath the skin, and factors such as skin hydration, and tissue curvature. Nevertheless, the calibration procedure is an effective way of computing probe coupling coefficients and obtain accurate estimates of tissue optical properties.

To validate the calibration process, we utilized one of the phantoms for the calibration process (Tab. 3.2), and verified it by estimating the optical properties on the other (Tab. 3.3). Tab. 3.4 summarizes the errors in optical properties retrieved from the Biomimic phantom (Tab. 3.3) based on the coupling coefficients estimated using the ISS phantom (Tab. 3.2). On

www.manaraa.com

average, the absolute error in measured optical properties was 8.6% and 19% in μ_a, and9.7% and 6% in μ_s' at 830 nm and 690 nm respectively.

Table 3.4: Percentage errors in estimates of μ_a and μ_s' from measurement of tissue simulating phantom (Tab. 3.3). Data was calibrated with measurements from (Tab. 3.2)

Detector	μ_a(830 nm)	μ_a(690 nm)	μ_s'(830 nm)	μ_s'(690 nm)
A	0.24	-14.91	-1.06	-6.38
B	-1.01	-17.68	-1.94	-1.38
C	-3.95	-16.24	4.02	-2.27
D	-2.71	-17.12	1.80	-0.65
E	-2.65	-21.38	-0.72	2.50
F	-6.75	-21.39	7.36	3.65
G	-8.87	-22.21	-1.38	1.85
H	-5.41	-19.88	3.65	-1.52

www.manaraa.com

CHAPTER 4: RESULTS AND DISCUSSION

4.1 Hemodynamic Changes due to Auditory Stimulation Measured with Modified Beer-Lambert Analysis

The results from Modified Beer-Lambert analysis of functional activation of the auditory cortex is summarized in this section. Recall that the Modified Beer-Lambert analysis estimates *changes* in concentrations of oxygenated hemoglobin (ΔC_{HbO}) and deoxygenated hemoglobin (ΔC_{HbR}) from optical intensity measurements at each source-detector separation. Hemodynamic responses were averaged across all 9 subjects for both stimuli - Broadband noise and 1000 Hz Pure-tone. As previously described in Sec. 3.1.3, the fiber optic probe manifold was positioned such that the sources were above the auditory cortex (T4), as shown in Fig. 4.1. The individual source-detector separations are given in table 3.1. Tables 4.1 and 4.2 compare the average hemodynamic response (*i.e.,* concentration changes ΔC_{HbO} and ΔC_{HbR} in μM) for each source-detector pair, and for both auditory stimuli. Thus, we can measure and compare the auditory hemodynamic response from 8 (detectors) $\times$ 4 (sources), encompassing the entire auditory cortex. The average response was estimated as the median of the concentration changes during auditory stimulation, *i.e.,* between time $t = 2$ s and $t = 10$ s. This ensures that the average estimates account for the rise time of functional hemodynamic changes. The median concentration change across 9 subjects, and the variance therein are reported. The statistical significance of the response was evaluated

www.manaraa.com

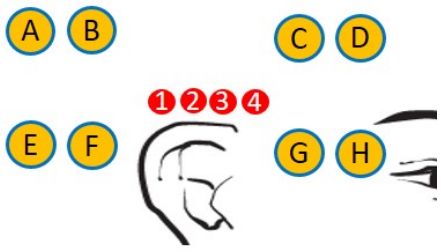

Figure 4.1: Schematic representing positioning of sources and detectors placed over the auditory cortex. The red circles at the center represent sources, placed above the Tragus and on the T4 position of the right ear. The yellow circles indicate the position of the detectors behind the ear and towards the forehead.

for each source-detector pair. Briefly, a non-parametric Wilcoxon signed rank tests were performed against the hypothesis that the concentration changes during functional activation were > 0. Statistically significant responses ($p < 0.05$) are marked with a $^{\#}$ in Tabs. 4.1 and 4.2.

From the Tab. 4.1, we note that in general the concentration of oxygenated hemoglobin (ΔC_{HbO}) increases due to functional activation. Further, in comparison to the results in Tab. 4.2, we observe that there is a greater change in concentration of oxygenated hemoglobin(ΔC_{HbO}), compared to deoxygenated hemoglobin (ΔC_{HbR}). On average, ΔC_{HbO} increases by $\sim 0.1 - 0.2\mu M$ due to functional activation. As expected, the response to auditory stimulation is not homogeneous across all source-detector separations. A highest ΔC_{HbO} response of 0.241 μM was observed during the presentation of the pure-tone stimulus, in Detector B and source 3. Further, only responses from source-detector pairs $A-2$, $A-3$, $B-2$, $B-3$, $B-4$, $C-2$, $D-1$, $E-3$and $F-1$ were found to be statistically significant. For Broadband noise stimulus, a highest ΔC_{HbO} concentration change of 0.196 μ M was observed in Detector H and source 1. Some source-detector pairs showed a statistically significant responses for ΔC_{HbR} for pure-tone stimulus.

www.manaraa.com

Table 4.1: Summary of average change in C_{HbO} (μM) due to auditory stimulation estimated using the Modified Beer-Lambert approach. Statistically significant responses are marked with a $^{\#}$.

Detector	Stimuli	Source 1	Source 2	Source 3	Source 4
A	pure-tone	0.005 ± 0.048	$0.071 \pm 0.082^{\#}$	$0.115 \pm 0.074^{\#}$	0.038 ± 0.077
	BBN	-0.029 ± 0.031	0.022 ± 0.065	0.061 ± 0.102	0.047 ± 0.061
B	pure-tone	0.011 ± 0.072	$0.135 \pm 0.116^{\#}$	$0.141 \pm 0.110^{\#}$	$0.053 \pm 0.084^{\#}$
	BBN	-0.029 ± 0.071	-0.019 ± 0.051	0.021 ± 0.054	0.026 ± 0.067
C	pure-tone	0.045 ± 0.077	$0.077 \pm 0.086^{\#}$	0.032 ± 0.118	0.051 ± 0.105
	BBN	0.074 ± 0.101	0.015 ± 0.088	0.036 ± 0.053	-0.015 ± 0.088
D	pure-tone	$0.136 \pm 0.112^{\#}$	0.061 ± 0.149	0.046 ± 0.152	0.066 ± 0.085
	BBN	0.002 ± 0.102	0.095 ± 0.072	0.077 ± 0.066	0.005 ± 0.072
E	pure-tone	0.003 ± 0.046	0.015 ± 0.037	$0.030 \pm 0.034^{\#}$	0.015 ± 0.035
	BBN	0.006 ± 0.053	-0.018 ± 0.067	-0.004 ± 0.073	0.002 ± 0.063
F	pure-tone	$-0.052 \pm 0.048^{\#}$	0.015 ± 0.038	0.030 ± 0.034	0.035 ± 0.015
	BBN	-0.028 ± 0.049	-0.012 ± 0.092	-0.024 ± 0.066	0.071 ± 0.086
G	pure-tone	0.042 ± 0.063	0.054 ± 0.077	0.035 ± 0.152	-0.051 ± 0.118
	BBN	-0.036 ± 0.066	-0.035 ± 0.075	-0.067 ± 0.076	0.049 ± 0.077
H	pure-tone	0.051 ± 0.041	0.034 ± 0.069	0.060 ± 0.088	-0.042 ± 0.075
	BBN	-0.104 ± 0.090	-0.076 ± 0.072	-0.098 ± 0.066	0.085 ± 0.075

www.manaraa.com

Table 4.2: Summary of average change in C_{HbR} (μM) due to auditory stimulation estimated using the Modified Beer-Lambert approach.

Detector	Stimuli	Source 1	Source 2	Source 3	Source 4
A	pure-tone	$0.014 \pm 0.0.035$	-0.007 ± 0.011	-0.0030 ± 0.022	$0.030 \pm 0.07528^{\#}$
	BBN	-0.013 ± 0.26	-0.020 ± 0.027	-0.006 ± 0.028	-0.020 ± 0.032
B	pure-tone	0.011 ± 0.028	-0.025 ± 0.027	-0.018 ± 0.033	0.021 ± 0.052
	BBN	-0.002 ± 0.034	-0.015 ± 0.029	-0.004 ± 0.024	-0.003 ± 0.036
C	pure-tone	0.006 ± 0.041	0.034 ± 0.069	-0.031 ± 0.054	-0.004 ± 0.046
	BBN	0.020 ± 0.048	0.041 ± 0.029	0.026 ± 0.031	0.020 ± 0.053
D	pure-tone	0.004 ± 0.070	0.0020 ± 0.038	0.013 ± 0.040	0.025 ± 0.034
	BBN	0.019 ± 0.071	0.021 ± 0.041	0.030 ± 0.047	0.022 ± 0.048
E	pure-tone	$0.047 \pm 0.017^{\#}$	$0.020 \pm 0.014^{\#}$	0.011 ± 0.018	$0.049 \pm 0.037^{\#}$
	BBN	-0.003 ± 0.027	0.004 ± 0.029	0.017 ± 0.014	0.005 ± 0.025
F	pure-tone	0.027 ± 0.025	$0.013 \pm 0.010^{\#}$	0.008 ± 0.025	$0.021 \pm 0.024^{\#}$
	BBN	0.001 ± 0.030	-0.001 ± 0.025	-0.006 ± 0.016	-0.017 ± 0.026
G	pure-tone	$0.024 \pm 0.016^{\#}$	0.015 ± 0.013	0.014 ± 0.015	-0.033 ± 0.038
	BBN	0.001 ± 0.051	0.015 ± 0.023	0.016 ± 0.022	-0.017 ± 0.026
H	pure-tone	0.008 ± 0.038	0.018 ± 0.015	0.015 ± 0.023	$0.039 \pm 0.038^{\#}$
	BBN	-0.023 ± 0.060	0.015 ± 0.024	0.019 ± 0.026	0.023 ± 0.026

www.manaraa.com

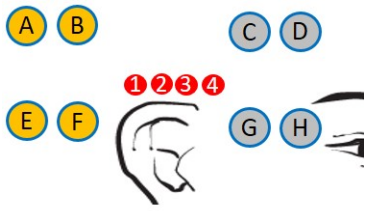

Figure 4.2: Placement of sources and detectors for the hemodynamic responses shown in Fig. 4.3.

4.1.1 Functional Activation Responses for Pure-tone Stimulus

We elaborate on the hemodynamic response due to functional activation with a pure-tone stimulus here. Fig. 4.3 shows the time courses of change in concentration of oxygenated and deoxygenated hemoglobin from the detectors towards the back of the head (*i.e.,* A, B, E, and F) for all four source positions. The sources are placed such that T4 region lies between the second and third source positions and two pairs of detectors are on either side of the T4 position. The positioning of these sources and detectors are highlighted in Fig. 4.2. Each panel of Fig. 4.3 displays the median (across all subjects) response of oxygenated hemoglobin (ΔC_{HbO}; solid red lines) and deoxygenated hemoglobin (ΔC_{HbR}; solid blue lines). The red and blue shaded regions highlight the upper and lower quartiles of the response. Vertical dotted lines represent the start and end of the stimulus.

From the graphs in Fig. 4.3 we observe that the concentration change during activation is prominent in Detectors A and B, across the sources 2, 3, and 4. There is approximately an increase of 0.2 μM in the concentration of the oxygenated hemoglobin. A small increase can be seen across the Detectors E and F at the third source position. These results suggest that region of activation is closer to the detectors A and B for pure-tone stimulus.

www.manaraa.com

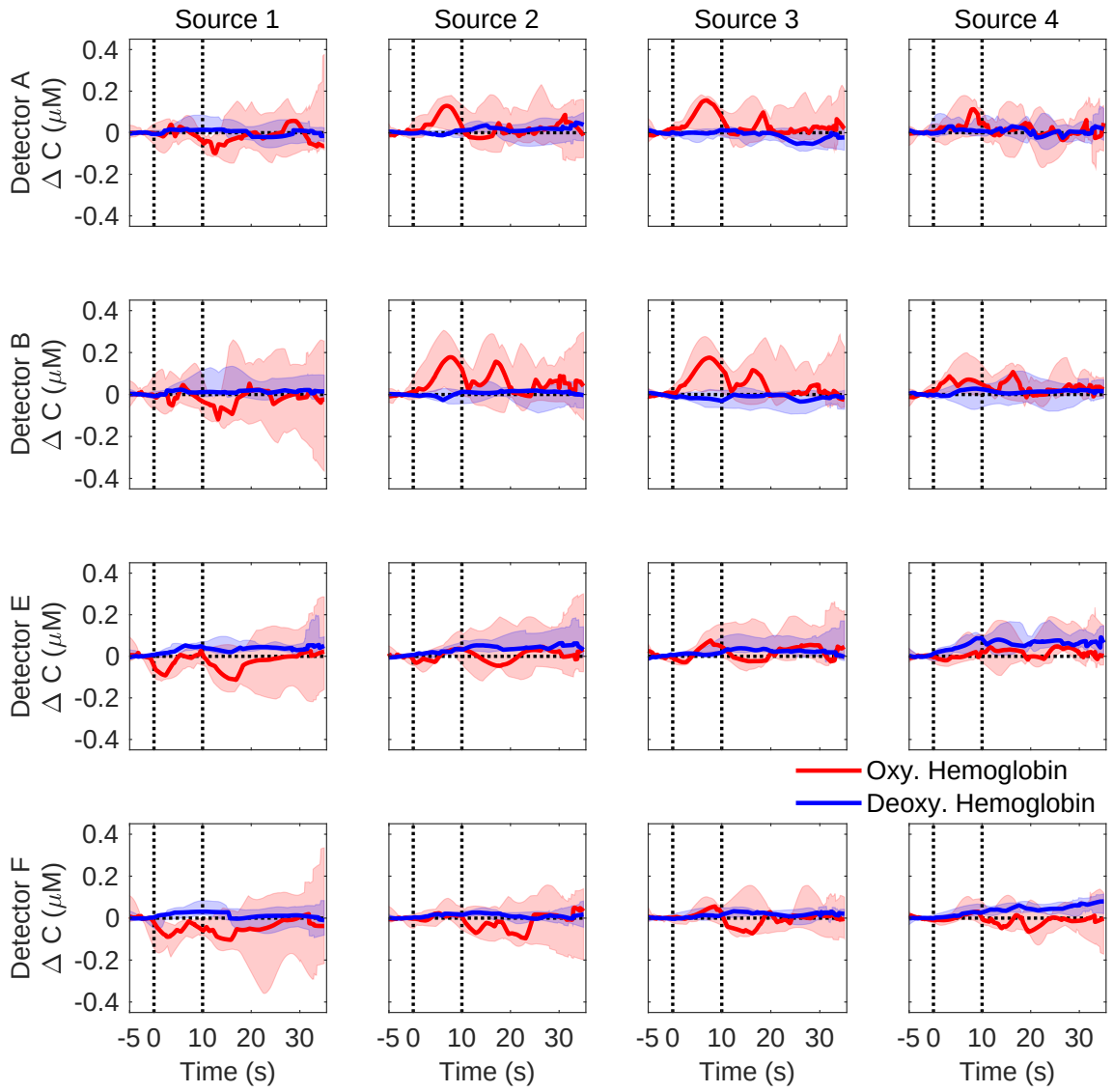

Figure 4.3: Changes in concentration of HbO (red) and HbR (blue) observed across the detectors A, B, E and F from all 4 source as shown in Fig. 4.2, for a pure-tone stimulus: Modified Beer-Lambert analysis. Solid lines indicate median responses from 9 subjects, and shaded regions highlight upper and lower quartile of responses. Vertical dotted lines represent the start and end time of the stimulus.

In a similar way, Fig. 4.5 shows the time courses of change in concentration of oxygenated and deoxygenated hemoglobin from the detectors towards the front of the head (*i.e.*,

www.manaraa.com

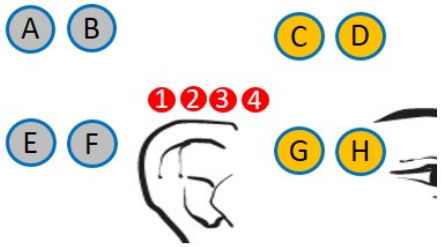

Figure 4.4: Position of the sources and detectors for the hemodynamic responses shown in Fig. 4.5.

C, D, G, and H) for all four source positions. The positioning of these sources and detectors are highlighted in Fig. 4.4. Each panel of Fig. 4.5 displays the median (across all subjects) response of oxygenated hemoglobin (ΔC_{HbO}; solid red lines) and deoxygenated hemoglobin (ΔC_{HbR}; solid blue lines). The red and blue shaded regions highlight the upper and lower quartiles of the response. Vertical dotted lines represent the start and end of the stimulus.

Fig. 4.5 shows a change in concentration of HbO across all detectors for sources 1, 2 and 3. The response at detectors C and detector G are greater compared to the detectors D and F, likely because they are located closer to the T4 region.

www.manaraa.com

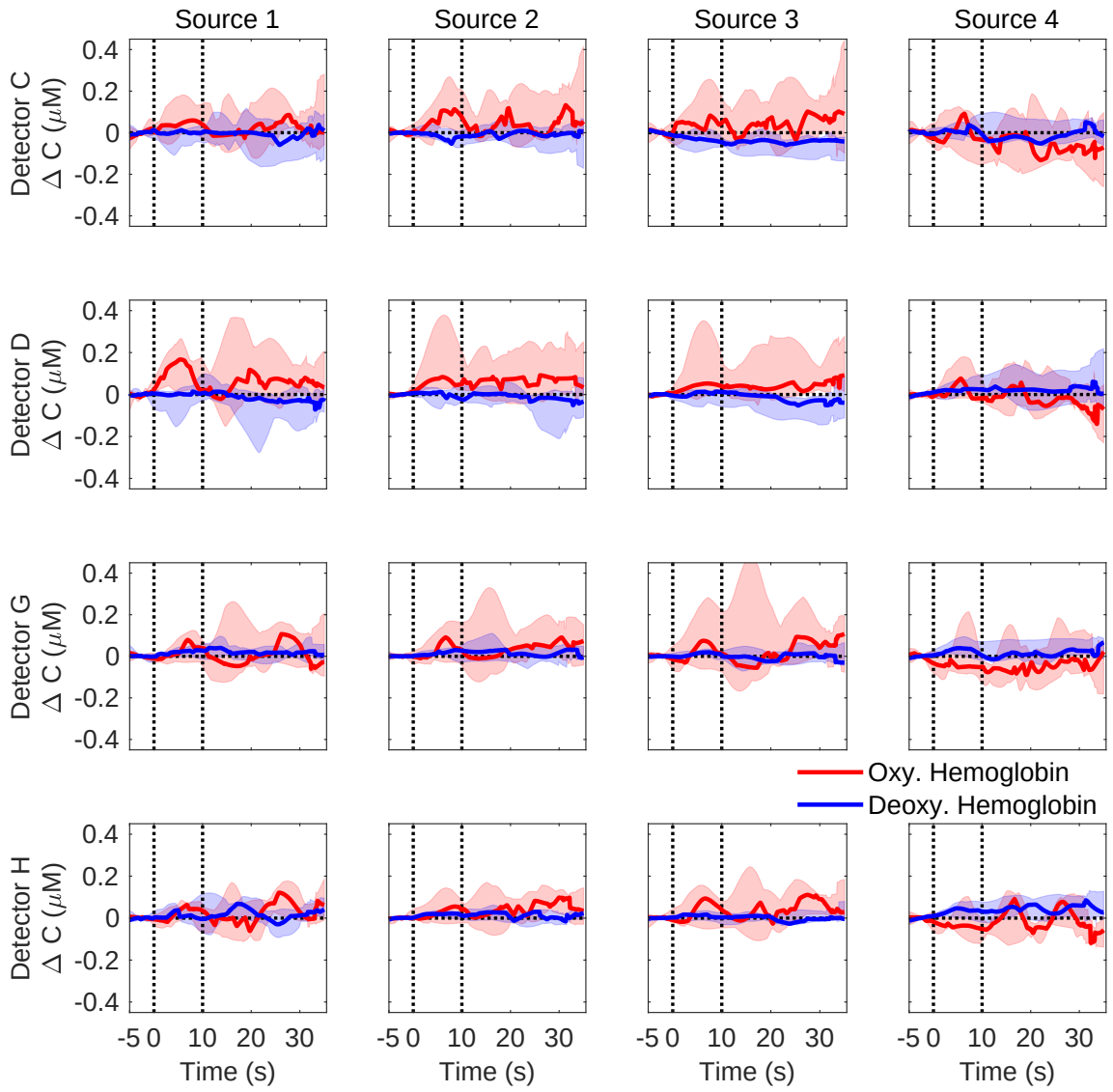

Figure 4.5: Changes in concentration of HbO (red) and HbR (blue) observed across the detectors C, D, G and H from all 4 source as shown in Fig. 4.4, for a pure-tone stimulus: Modified Beer-Lambert analysis. Solid lines indicate median responses from 9 subjects, and shaded regions highlight upper and lower quartile of responses. Vertical dotted lines represent the start and end time of the stimulus.

www.manaraa.com

4.1.2 Functional Activation Responses for Broadband Stimulus

Fig. 4.6 and 4.7 show the changes in concetration of oxygenated and deoxygenated hemoglobin for detectors A, B, E & F, and C, D, G & H respectively, for all 4 source positions. In this case, 70 dB SPL Broadband noise was presented. The positioning of sources and detectors are highlighted in the schematics Fig. 4.2 and Fig. 4.4 respectively. As before, the median changes in concentration of HbO and HbR are indicated in solid red and blue lines respectively. Shaded regions indicate upper and lower quantiles of the response, and vertical dotted lines indicate period of activation. From these graphs, we note a concentration change across all the detectors for sources 2, 3 and 4. This indicates a larger activation area, consistent with the physiological expectation for stimulation from a Broadband sound.

www.manaraa.com

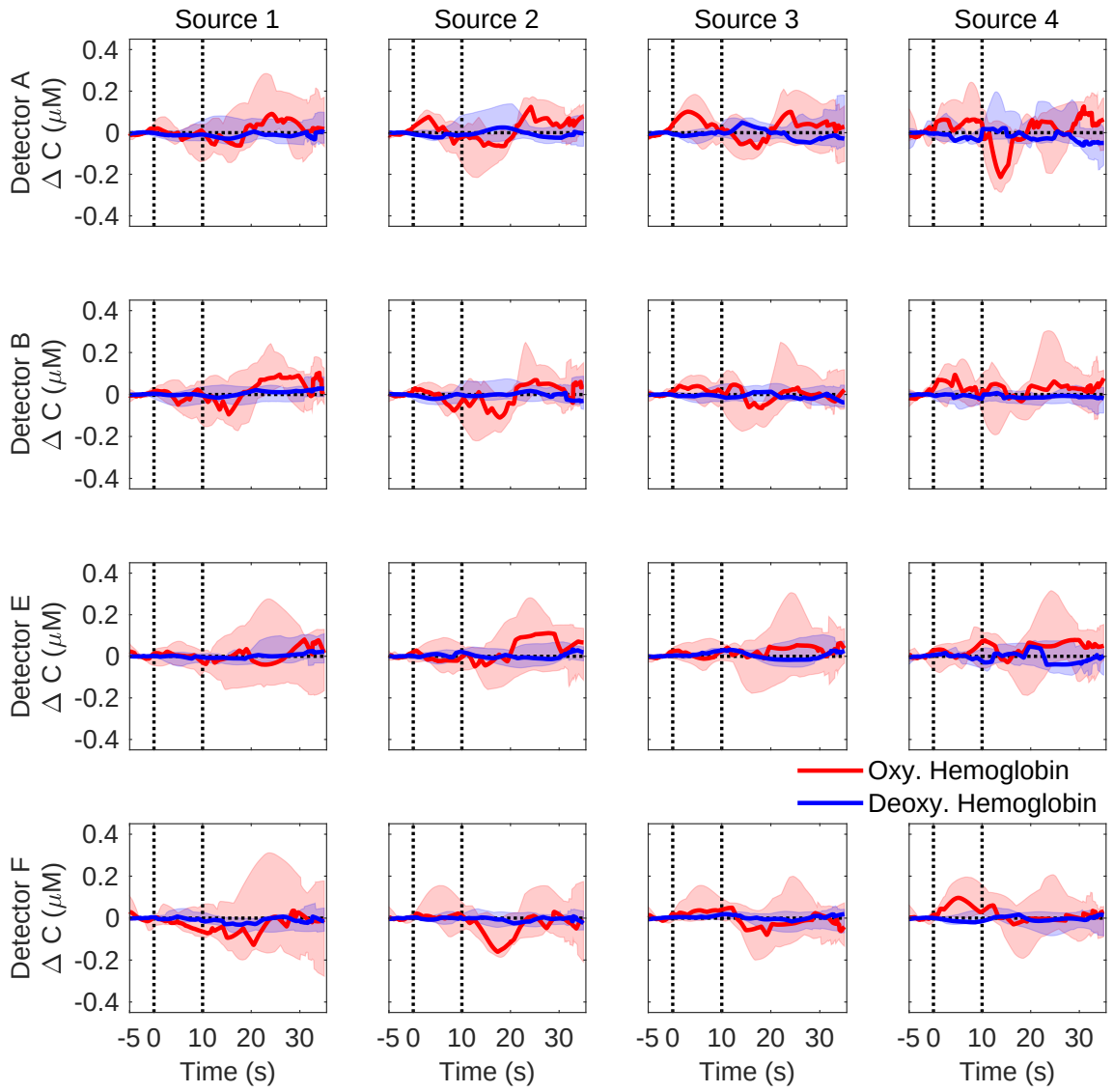

Figure 4.6: Changes in concentration of HbO (red) and HbR (blue) observed across the detectors A, B, E and F from all 4 source as shown in Fig. 4.2, for a broadband noise (70 dB SPL): Modified Beer-Lambert analysis. Solid lines indicate median responses from 9 subjects, and shaded regions highlight upper and lower quartile of responses. Vertical dotted lines represent the start and end time of the stimulus.

www.manaraa.com

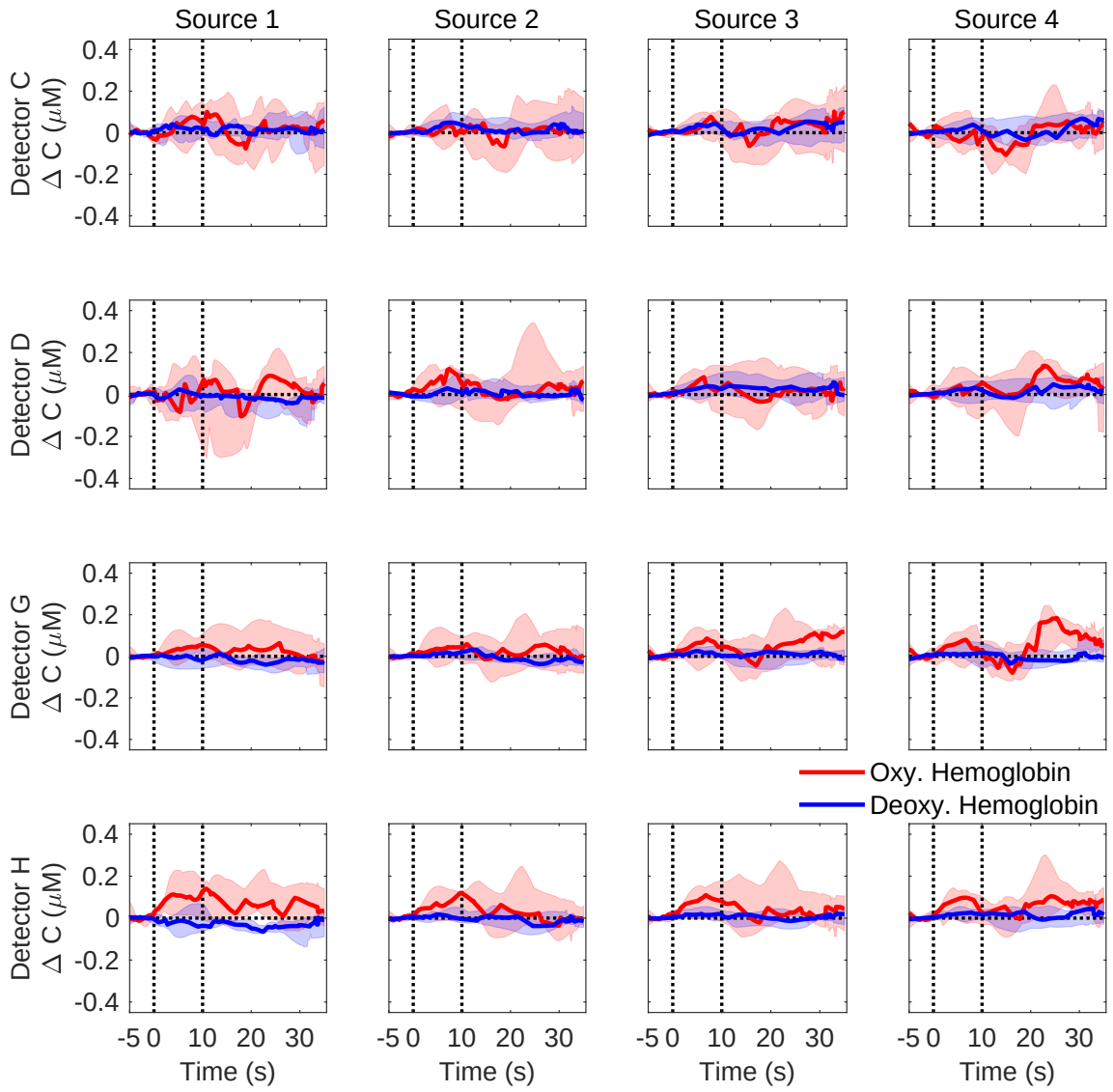

Figure 4.7: Changes in concentration of HbO (red) and HbR (blue) observed across the detectors C, D, G and H from all 4 source as shown in Fig. 4.4, for a broadband noise (70 dB SPL): Modified Beer-Lambert analysis. Solid lines indicate median responses from 9 subjects, and shaded regions highlight upper and lower quartile of responses. Vertical dotted lines represent the start and end time of the stimulus.

www.manaraa.com

4.2 Hemodynamic Changes due to Auditory Stimulation Measured with FD-NIRS Analysis

Tab. 4.3 shows the average change in concentration of C_{HbO} and C_{HbR} from all 8 detectors using the multi-distance FD-NIRS method 2.4. The average response was estimated as the median of the concentration changes during auditory stimulation, *i.e.,* between time $t = 2$ s and $t = 10$ s. Recall that the multi-distance FD-NIRS approach analyzes optical measurements obtained from *all* sources to arrive at a single time course per detector. For FD-NIRS analysis, results from three subjects were excluded. One subject's data was unusable due to large errors during the calibration process. Data from two more subjects were excluded because of saturation warnings during the experiment. Since FD-NIRS measurements require reliable data from all source-detector positions, analysis of the saturated measurements yielded non-physiological functional activation responses. Thus, results shown in this section are averaged responses across 6 subjects. From Tab. 4.3 we observe that for pure-tone stimulus, ΔC_{HbO} increases to a highest value of 0.785 μM and ΔC_{HbR} decreases to a minimum of 0.051 μM over the span of 10 s stimulus presentation. Similarly during the presentation of Broadband noise, ΔC_{HbO} increased to a highest value of 0.373 μM and ΔC_{HbO} decreased to a minimum of 0.051 μM.

Figs. 4.8 and 4.9 show the changes in the concentration of ΔC_{HbO} and ΔC_{HbR} from all detectors for pure-tone and Broadband noise respectively. As before, the median changes in concentration of HbO and HbR are indicated in solid red and blue lines respectively. Shaded regions indicate upper and lower quantiles of the response, and vertical dotted lines indicate period of activation. For both stimuli, measurements from the farthest detectors

www.manaraa.com

(*i.e.*, A, E, D, and H) were noisy and generally unreliable. This is likely due to reduced signal intensities from the longer source-detector separations. Moderate, but non statistically significant (Wilcoxon signed rank test) increases in ΔC_{HbO} were observed in detector B for pure-tone stimulus, and detectors C, F and G for Broadband noise.

Table 4.3: Summary of average change in C_{HbO} (μM) and C_{HbR} (μM) due to auditory stimulation estimated using the multi-distance FD-NIRS approach.

Detector	Pure-tone		BBN	
	HbO	HbR	HbO	HbR
A	-0.401 ± 0.384	0.009 ± 0.288	0.274 ± 0.099	0.201 ± 0.104
B	0.113 ± 0.156	0.092 ± 0.162	0.023 ± 0.131	0.020 ± 0.038
C	-0.085 ± 0.230	0.037 ± 0.3080	-0.002 ± 0.161	-0.015 ± 0.096
D	-0.031 ± 0.358	0.012 ± 0.127	-0.067 ± 0.275	0.034 ± 0.100
E	0.178 ± 0.061	-0.153 ± 0.224	0.104 ± 0.179	0.013 ± 0.090
F	0.034 ± 0.064	-0.015 ± 0.036	0.120 ± 0.013	0.011 ± 0.054
G	0.109 ± 0.102	-0.042 ± 0.090	0.050 ± 0.117	-0.045 ± 0.006
H	-0.018 ± 0.124	0.046 ± 0.106	-0.104 ± 0.182	0.106 ± 0.126

www.manaraa.com

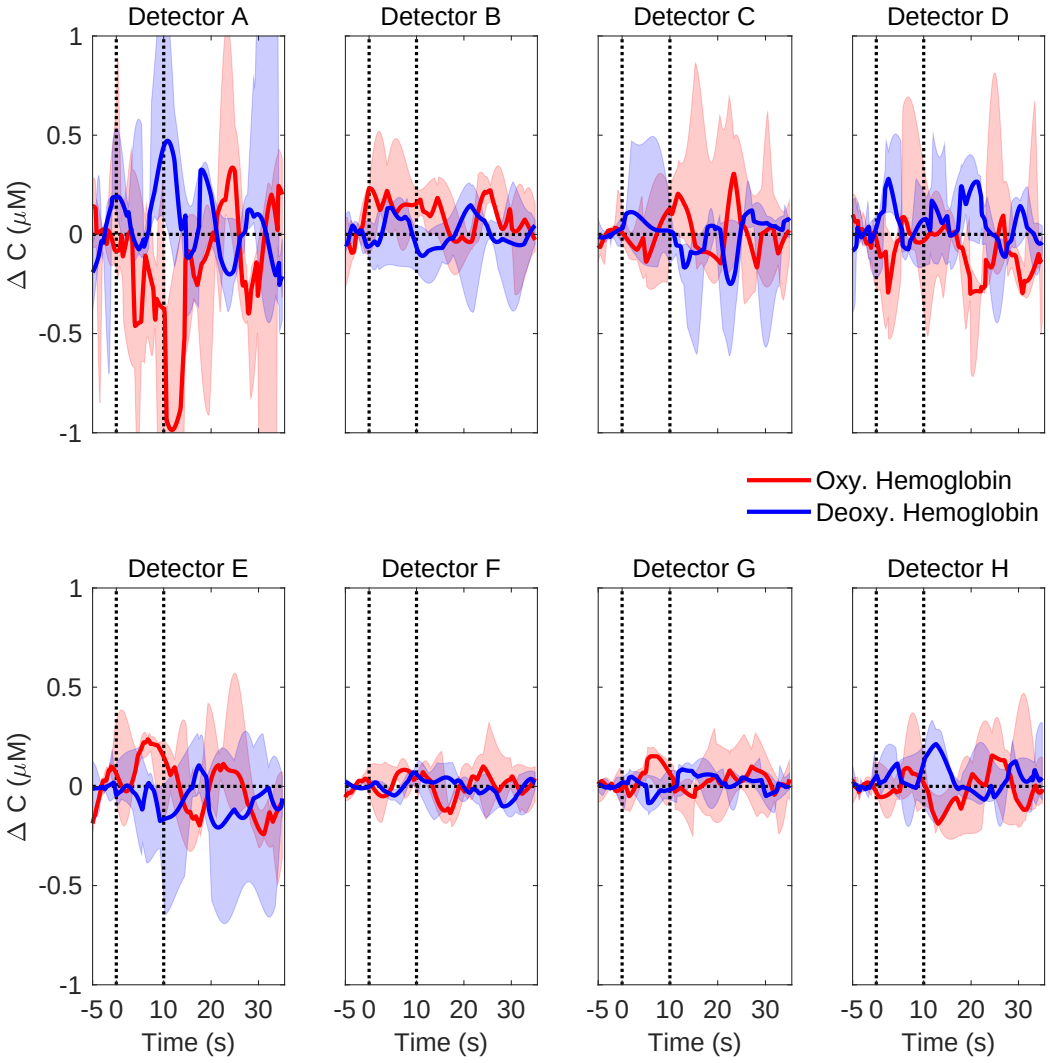

Figure 4.8: Changes in concentration of HbO (red) and HbR (blue) observed across 8 detectors for a 1000 Hz pure-tone: FD-NIRS analysis. Solid lines indicate median responses from 6 subjects, and shaded regions highlight upper and lower quartile of responses. Vertical dotted lines represent the start and end time of the stimulus.

www.manaraa.com

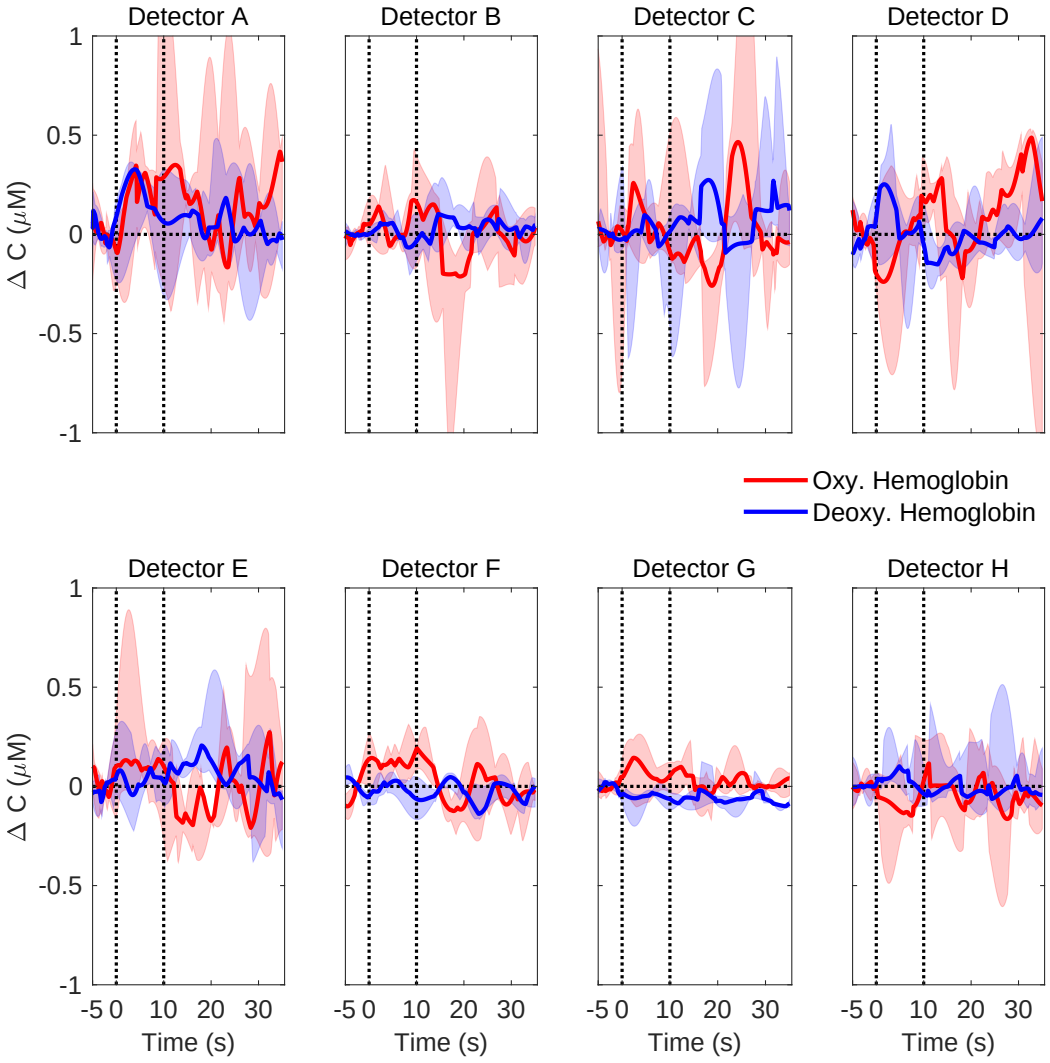

Figure 4.9: Changes in concentration of *HbO* (red) and *HbR* (blue) observed across 8 detectors for a broadband noise (70 dB SPL): FD-NIRS analysis. Solid lines indicate median responses from 6 subjects, and shaded regions highlight upper and lower quartile of responses. Vertical dotted lines represent the start and end time of the stimulus.

4.3 Discussion

The overall goal of this thesis is to verify if the multi-distance FD-NIRS method can identify/measure hemodynamic changes due to functional activation, and compare results

www.manaraa.com

therein to the conventional CW-NIRS (Modified Beer-Lambert law) approach. To effect this comparison, we compared the hemodynamic responses (ΔC_{HbO} and ΔC_{HbR}) obtained via the frequency domain method with the 'best' and 'average' hemodynamic responses obtained via Modified Beer-Lambert analysis. Here, 'best' response refers to the source-detector separation that provides the clearest/largest hemodynamic response. 'Average' response refers to the average of hemodynamic responses from all sources for a given detector. Since they use measurements from all sources, the 'average' response should be similar to the results obtained via the FD-NIRS method.

Tabs. 4.4 and 4.5 compare respectively the average HbO and HbR functional activation response from all detectors for both auditory stimuli. Here, we observe that the median responses are highest for the 'best' single distance measurements. Results from the average response of all sources (modified Beer-Lambert) were similar to the responses obtained from FD-NIRS. For pure-tone, the highest FD-NIRS HbO response was observed in detectors B and E, whereas the highest HbO response was observed in detector B for both 'best' and 'average' single distance measurements. For Broadband noise, the highest FD-NIRS HbO response was observed in detector A , whereas the highest HbO response was observed in detectors F and H with the 'best' and 'average' single distance measurements.

www.manaraa.com

Table 4.4: Summary of average change in C_{HbO} (μM) due to auditory stimulation from the 'best' single-distance measurement (MBL), 'average' of all single-distance measurements (MBL), and from multi-distance FD-NIRS approach, for both pure-tone and broadband noise.

Detector	Stimulus	Best separation	Average change	FD-NIRS
A	pure-tone	0.082 ± 0.071	0.079 ± 0.058	-0.401 ± 0.384
	BBN	0.053 ± 0.079	0.030 ± 0.065	0.274 ± 0.099
B	pure-tone	0.135 ± 0.116	0.100 ± 0.075	0.113 ± 0.156
	BBN	0.041 ± 0.062	0.012 ± 0.053	0.023 ± 0.131
C	pure-tone	0.032 ± 0.118	0.03 ± 0.108	-0.085 ± 0.23
	BBN	0.018 ± 0.042	0.00 ± 0.064	-0.002 ± 0.161
D	pure-tone	0.046 ± 0.152	0.030 ± 0.132	-0.031 ± 0.358
	BBN	0.061 ± 0.062	0.093 ± 0.080	-0.067 ± 0.275
E	pure-tone	0.015 ± 0.037	-0.002 ± 0.040	0.178 ± 0.061
	BBN	0.012 ± 0.057	-0.003 ± 0.053	0.104 ± 0.179
F	pure-tone	0.015 ± 0.038	0.006 ± 0.021	0.034 ± 0.064
	BBN	0.060 ± 0.084	0.001 ± 0.050	0.120 ± 0.013
G	pure-tone	0.035 ± 0.152	0.039 ± 0.093	0.109 ± 0.102
	BBN	0.063 ± 0.064	0.043 ± 0.064	0.050 ± 0.117
H	pure-tone	0.060 ± 0.088	0.057 ± 0.059	0.018 ± 0.124
	BBN	0.080 ± 0.062	0.099 ± 0.084	-0.104 ± 0.182

www.manaraa.com

Table 4.5: Summary of average change in C_{HbR} (μM) due to auditory stimulation from the 'best' single-distance measurement (MBL), 'average' of all single-distance measurements (MBL), and from multi-distance FD-NIRS approach, for both pure-tone and broadband noise.

Detector	Stimulus	Best separation	Average change	FD-NIRS
A	pure-tone	-0.007 ± 0.011	-0.07 ± 0.011	0.09 ± 0.288
	BBN	-0.008 ± 0.042	-0.007 ± 0.021	0.201 ± 0.104
B	pure-tone	-0.025 ± 0.027	0.014 ± 0.032	0.092 ± 0.162
	BBN	-0.010 ± 0.029	-0.010 ± 0.028	0.020 ± 0.038
C	pure-tone	-0.031 ± 0.054	-0.017 ± 0.026	0.037 ± 0.308
	BBN	0.023 ± 0.026	0.0250 ± 0.016	-0.015 ± 0.096
D	pure-tone	0.013 ± 0.040	0.016 ± 0.038	0.012 ± 0.127
	BBN	0.027 ± 0.043	0.006 ± 0.051	0.034 ± 0.100
E	pure-tone	0.020 ± 0.014	0.031 ± 0.018	-0.153 ± 0.224
	BBN	0.007 ± 0.016	0.003 ± 0.020	0.13 ± 0.090
F	pure-tone	$0.0.013 \pm 0.010$	0.019 ± 0.022	-0.015 ± 0.036
	BBN	-0.016 ± 0.021	0.09 ± 0.12	0.011 ± 0.054
G	pure-tone	0.014 ± 0.015	0.020 ± 0.018	-0.042 ± 0.090
	BBN	0.14 ± 0.019	0.008 ± 0.022	-0.045 ± 0.006
H	pure-tone	0.0015 ± 0.023	0.018 ± 0.024	0.046 ± 0.106
	BBN	0.019 ± 0.025	0.017 ± 0.029	0.106 ± 0.126

www.manaraa.com

Figs. 4.10 and 4.11 show a comparison of hemodynamic responses from detectors closest to the sources for pure-tone and Broadband noise stimuli. Each row represents the responses from 4 detectors, *i.e.,* B, F, C, and G. The columns represent three analysis methods - 'best' single-distance CW-NIRS measurements, 'average' of all CW-NIRS measurements, and 'FD-NIRS' measurements. Median concentration changes ΔC_{HbO} and ΔC_{HbR} curves are represented as solid red and blue curves respectively. Shaded regions highlight upper and lower quantiles, while vertical dotted lines indicate activation duration.

For pure-tone stimulus, detector B shows an observable and consistent change in concentration of HbO for the best single distance measurement (source 2). This response is attenuated in both the averaged measurements and in FD-NIRS. The response from other detectors are minimal. For Broadband noise, a good response is seen across the detectors B and F for the best single distance case (source 4) and a moderate response across detectors C and G (source 3). We observe that the responses from the FD-NIRS approach is more noisy compared to the modified Beer-Lambert approach.

www.manaraa.com

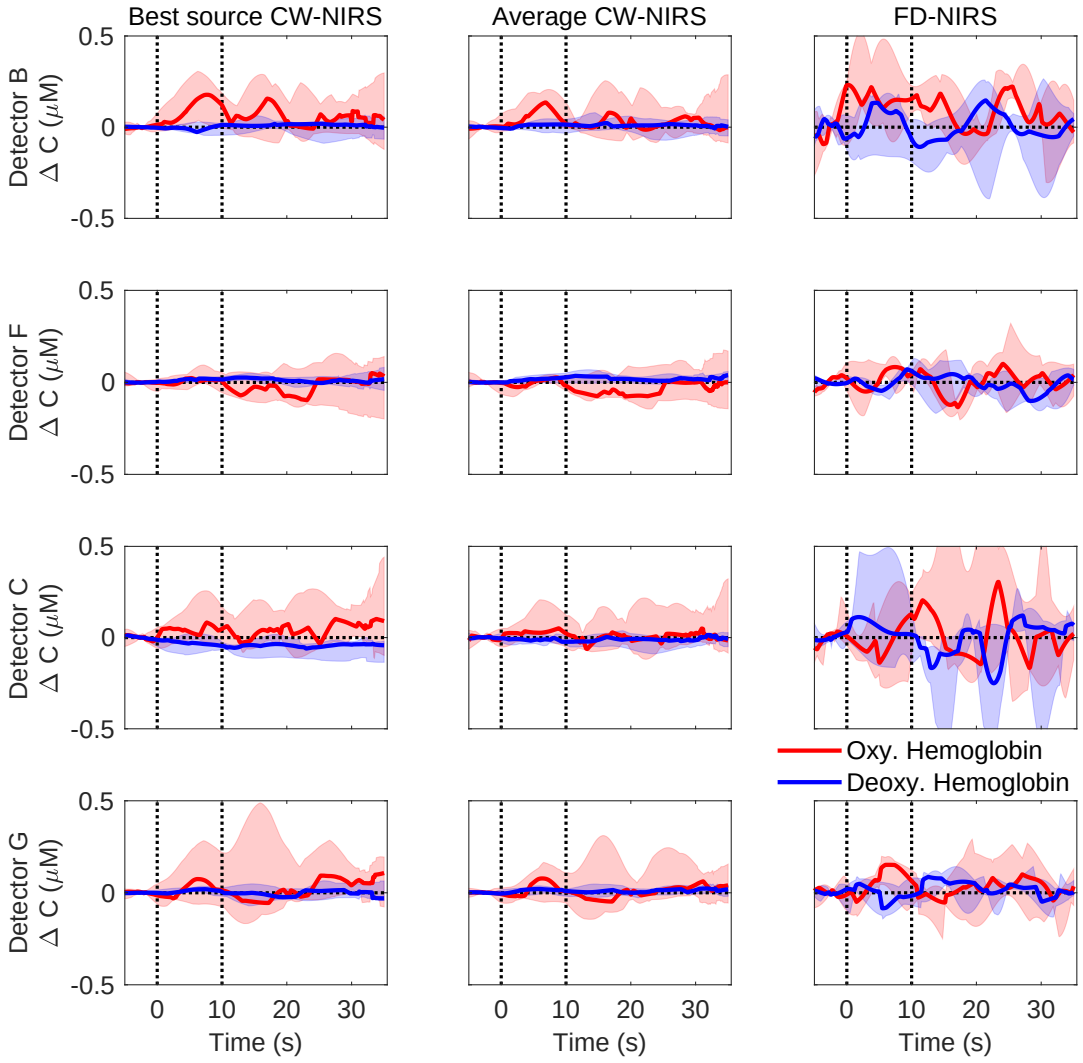

Figure 4.10: Comparison of responses from the Modified Beer-Lambert analysis and the FD-NIRS analysis for pure-tone stimulus. Each row represents the detector being analyzed. The first column shows the best response observed across the detector for one single source-detector separation (source 2 for detectors B and F, and source 3 for detectors C and G). The second column displays the average response observed across all the sources for that detector, while the third column displays FD-NIRS results. The position of these detectors is shown in Fig. 4.1. Solid red and blue lines indicate medial HbO and HbR responses, shaded regions are upper and lower quantiles, and dotted lines are stimulus duration.

www.manaraa.com

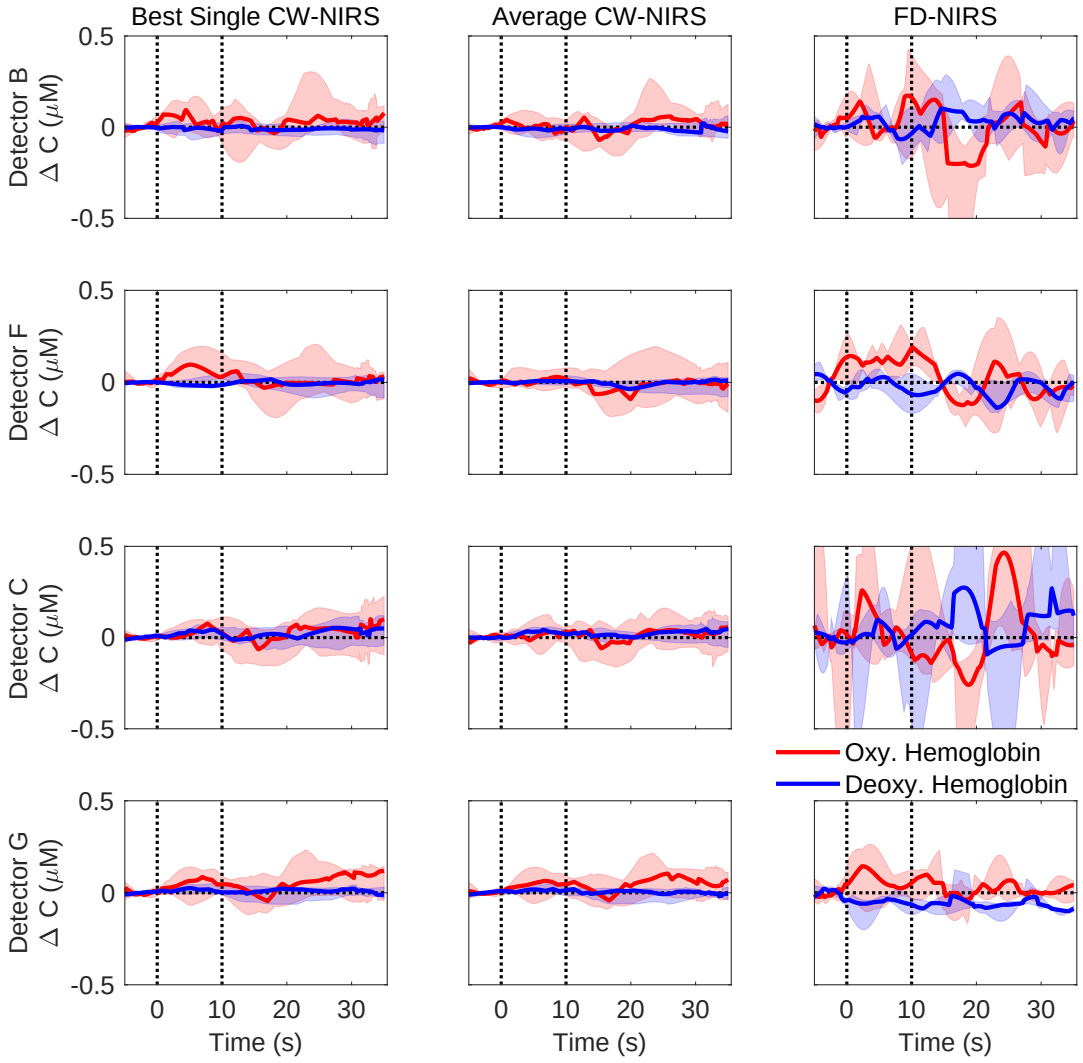

Figure 4.11: Comparison of responses from the Modified Beer-Lambert analysis and the FD-NIRS analysis for broadband noise. Each row represents the detector being analyzed. The first column shows the best response observed across the detector for one single source-detector separation (source 4 for detectors B and F, and source 3 for detectors C and G). The second column displays the average response observed across all the sources for that detector, while the third column displays FD-NIRS results. The position of these detectors is shown in Fig. 4.1. Solid red and blue lines indicate medial HbO and HbR responses, shaded regions are upper and lower quantiles, and dotted lines are stimulus duration.

www.manaraa.com

From the results, we see that there is a large difference the ranges of different analysis approaches. Previous studies of Chen et. al. [11] reported a maximum change in concentration of HbO of 0.4 μM. Wiggings et. al. [43] and Issa et. al. [27] reported a maximum change of 0.1 μM. The results obtained here by the modified Beer-Lambert approach are consistent with limited previous research. FD-NIRS analysis, show a higher measured concentration changes of HbO, but with significantly higher noise in measurements.

To our knowledge, this is the first study to use the multi-distance frequency domain method to record hemodynamic changes due to functional activation of the auditory cortex. One of the reasons for this unconventional performance of the multi distance FD-NIRS method could be due the analysis technique requiring measurements from several source-detector pairs. Recall that a linear fit performed for the estimation of k_r and k_i values (Fig. 4.12). With this analysis method, the tissue sampling volume of a single measurement is larger than a single distance (CW-NIRS) measurement. Functional activation is related to neuronal activity taking place in a specific region *i.e., focal* region of the brain rather than *i.e., global* that occur over the entire brain (*e.g.,* hypoxia). When we perform a linear fit for the values of $log(\rho^2 A(\rho))$ and $\theta(\rho)$ to measure the κ_r and κ_i values, it is therefore possible that the functional stimulation only effects changes at one or two source detector separations, with minimal changes across the other separations (within noise). So, a linear fit of such a local change may tend to suppress/underestimate the hemodynamic change resulting in the loss of the response from the detector. From the Fig. 4.12, we can see the possibility of suppression in activation measured at some source detector separations due the linear fit performed. Thus, although the multi-distance FD-NIRS system has the advantage of measuring the absolute concentrations of HbO and HbR, it is likely more beneficial to

www.manaraa.com

use this approach for conditions that involve *global* changes such as hypoxia or ischemia, compared to the *focal* changes such as functional activation.

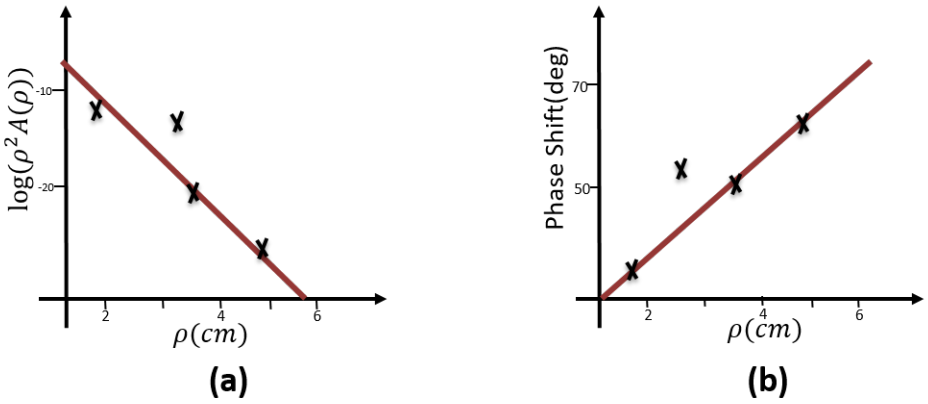

Figure 4.12: A linear fit being performed for four source detector separations, with a hypothetical functional activation change at one separation. A linear fit could suppress/underestimate the measurement at the second source detector separation in the *(a.)* amplitude and *(b.)* phase while estimating κ_r and κ_i

4.3.1 Limitations and Sources of Error

We note several limitations that were present in our study.

4.3.1.1 Density of Hair Roots

Hair absorbs near infrared light, and has an effect of attenuating measured signals. The amount of hair present, *i.e.,* the density of the hair roots on the scalp, present between the detector and scalp effected the measurements in a considerable way. In order to reduce the impact of hair, the detector and the source positions were thoroughly checked each time for the presence of hair. Efforts were made to brush/move hair away from the detector fiber to ensure optimal fiber/scalp contact. We were able to recover good responses from subjects having hair with low levels of dark pigment eumelanin (blonde hair) compared to the subjects with darker hair. Despite these efforts, absorption of light by hair follicles was unavoidable.

www.manaraa.com

4.3.1.2 Scalp and Fiber Coupling

To solve for the coupling, as mentioned in Sec. 3.3.1, calibration was performed using two solid phantoms. Using the ISS phantom provided by ISS.inc as a reference phantom we applied the calibration co efficients of ISS phantom to measure the optical properties of the Biomimic phantom. If the optical properties recovered was within 20% expected values, the same co-efficients were used to calibrate for the subject data. During the experiments, one of the datasets had a large error ($> 20\%$) in the calibration error measured, so this was excluded from the frequency domain results.

4.3.1.3 Positioning of T4 on Scalp

Identifying and positioning the source over T4 on the scalp was important for comparing measurements over all subjects. In order to accomplish this, measurements of the head were made using a measuring tape, *i.e.,* diameter of the head was measured, the distance from Inion to Nasion, and from Right Tragus to Left Tragus was measured. T4was located by calculating 10% of the distance from Right - Left Targus. Various layouts of probes were tested for optimal probe contact, flexibility. The distances between the sources and detectors in these designs were also optimized to track good responses.

4.3.1.4 Motion Artifact Correction

Motion artifacts (*e.g.,* due to coughing) change the fiber-scalp coupling and location, and could affect the estimated concentrations. The subjects were instructed to remain still during the experiments and were asked to have as little movement as possible. Even after taking necessary precautions the data had few major artifacts, therefore, a four point moving

www.manaraa.com

average filter was used to identify and remove trials that exhibit these effects. Nevertheless, the presence of smaller artifacts will affect the fidelity of the data.

4.3.2 Future Work

One interesting result from this research is the experimental comparison of multi-distance and single-distance analysis of optical functional activation measurements, which suggests that focal changes in hemodynamics may be underestimated by multi-distance techniques such as FD-NIRS. For further investigation and confirmation of this hypothesis, a future direction of research would be to perform a numerical simulation of functional activation (*e.g.,* using NIRFAST[13]), and perform single- and multi-distance analysis of the simulated data. Calculated responses from simulated data can be compared with simulation parameters, and experimental results. One other future direction would be to extend this study to include subjects with tinnitus to observe the trend of activation in them and compare it with responses from the healthy subjects.

www.manaraa.com

CHAPTER 5: CONCLUSION

Functional stimulation of the auditory cortex was studied using Near-Infrared Spectroscopy. A comparison of the two types of optical analysis was performed. Multi-Distance Frequency Domain analysis of the data yielded baseline measurements of oxygenated and deoxygenated hemoglobin, while single-distance Modified Beer-Lambert analysis yielded measurements of changes in oxygenated and deoxygenated hemoglobin. Modified Beer-Lambert analysis estimated larger changes in hemoglobin concentrations when compared to the Frequency domain analysis. Results suggest that single distance analysis approaches may be better suited to measure focal changes due to functional activation.

www.manaraa.com

REFERENCES

[1] Simon R Arridge, M Cope, and DT Delpy. The theoretical basis for the determination of optical pathlengths in tissue: temporal and frequency analysis. *Physics in Medicine & Biology*, 37(7):1531, 1992.

[2] Simon R Arridge and William RB Lionheart. Nonuniqueness in diffusion-based optical tomography. *Optics letters*, 23(11):882–884, 1998.

[3] Wesley Boehs Baker. *Optical cerebral blood flow monitoring of mice to men*. PhD thesis, University of Pennsylvania, 2015.

[4] Jeffrey W. Barker, Ashok Panigrahy, and Theodore J. Huppert. Accuracy of oxygen saturation and total hemoglobin estimates in the neonatal brain using the semi-infinite slab model for FD-NIRS data analysis. *Biomedical Optics Express*, 5(12):4300.

[5] Jay M Bhatt, Harrison W Lin, and Neil Bhattacharyya. Prevalence, severity, exposures, and treatment patterns of tinnitus in the united states. *JAMA Otolaryngology–Head & Neck Surgery*, 142(10):959–965, 2016.

[6] Irving J Bigio and Sergio Fantini. *Quantitative Biomedical Optics: Theory, Methods, and Applications*. Cambridge University Press, 2016.

[7] DA Boas, MA O'leary, B Chance, and AG Yodh. Scattering of diffuse photon density waves by spherical inhomogeneities within turbid media: analytic solution and applications. *Proceedings of the National Academy of Sciences*, 91(11):4887–4891, 1994.

[8] Sabrina Brigadoi, Lisa Ceccherini, Simone Cutini, Fabio Scarpa, Pietro Scatturin, Juliette Selb, Louis Gagnon, David A Boas, and Robert J Cooper. Motion artifacts in functional near-infrared spectroscopy: a comparison of motion correction techniques applied to real cognitive data. *NeuroImage*, 85:181–191, 2014.

[9] Erin M Buckley. *Cerebral hemodynamics in high-risk neonates probed by diffuse optical spectroscopies*. PhD thesis, University of Pennsylvania, 2011.

www.manaraa.com

[10] Mateo Calderon-Arnulphi, Ali Alaraj, Sepideh Amin-Hanjani, William W Mantulin, Chiara M Polzonetti, Enrico Gratton, and Fady T Charbel. Detection of cerebral ischemia in neurovascular surgery using quantitative frequency-domain near-infrared spectroscopy. *Journal of neurosurgery*, 106(2):283–290, 2007.

[11] Ling-Chia Chen, Pascale Sandmann, Jeremy D. Thorne, Christoph S. Herrmann, and Stefan Debener. Association of concurrent fNIRS and EEG signatures in response to auditory and visual stimuli. *Brain Topography*, 28(5):710–725.

[12] David James Davies, Michael Clancy, Daniel Lighter, George M. Balanos, Samuel John Edwin Lucas, Hamid Dehghani, Zhangjie Su, Mario Forcione, and Antonio Belli. Frequency-domain vs continuous-wave near-infrared spectroscopy devices: a comparison of clinically viable monitors in controlled hypoxia. *Journal of Clinical Monitoring and Computing*, 31(5):967–974.

[13] Hamid Dehghani, Matthew E Eames, Phaneendra K Yalavarthy, Scott C Davis, Subhadra Srinivasan, Colin M Carpenter, Brian W Pogue, and Keith D Paulsen. Near infrared optical tomography using nirfast: Algorithm for numerical model and image reconstruction. *International Journal for Numerical Methods in Biomedical Engineering*, 25(6):711–732, 2009.

[14] David T Delpy, Mark Cope, Pieter van der Zee, SR Arridge, Susan Wray, and JS Wyatt. Estimation of optical pathlength through tissue from direct time of flight measurement. *Physics in Medicine & Biology*, 33(12):1433, 1988.

[15] Anna Devor, Sava Sakadžić, Vivek J Srinivasan, Mohammad A Yaseen, Krystal Nizar, Payam A Saisan, Peifang Tian, Anders M Dale, Sergei A Vinogradov, Maria Angela Franceschini, et al. Frontiers in optical imaging of cerebral blood flow and metabolism. *Journal of Cerebral Blood Flow & Metabolism*, 32(7):1259–1276, 2012.

[16] Edgar A DeYoe, Peter Bandettini, Jay Neitz, David Miller, and Paula Winans. Functional magnetic resonance imaging (fmri) of the human brain. *Journal of neuroscience methods*, 54(2):171–187, 1994.

[17] Arlene Duncan, Judith H Meek, Matthew Clemence, Clare E Elwell, Lidia Tyszczuk, Mark Cope, and D Delpy. Optical pathlength measurements on adult head, calf and forearm and the head of the newborn infant using phase resolved optical spectroscopy. *Physics in Medicine & Biology*, 40(2):295, 1995.

[18] Turgut Durduran. Noninvasive measurements of tissue hemodynamics with hybrid diffuse optical methods. *Medical Physics*, 31(7):2178–2178.

[19] Turgut Durduran, Regine Choe, WB Baker, and Arjun G Yodh. Diffuse optics for tissue monitoring and tomography. *Reports on Progress in Physics*, 73(7):076701, 2010.

www.manaraa.com

[20] Sergio Fantini, Maria-Angela Franceschini, John S Maier, Scott A Walker, Beniamino B Barbieri, and Enrico Gratton. Frequency-domain multichannel optical detector for non-invasive tissue spectroscopy and oximetry. *Optical Engineering*, 34(1):32–43, 1995.

[21] Sergio Fantini, Dennis Hueber, Maria Angela Franceschini, Enrico Gratton, Warren Rosenfeld, Phillip G Stubblefield, Dev Maulik, and Miljan R Stankovic. Non-invasive optical monitoring of the newborn piglet brain using continuous-wave and frequency-domain spectroscopy. *Physics in medicine and biology*, 44(6):1543–1563.

[22] Maria Angela Franceschini and David A Boas. Noninvasive measurement of neuronal activity with near-infrared optical imaging. *Neuroimage*, 21(1):372–386, 2004.

[23] Angela R. Harrivel, Daniel H. Weissman, Douglas C. Noll, and Scott J. Peltier. Monitoring attentional state with fNIRS. *Frontiers in Human Neuroscience*, 7.

[24] Keum-Shik Hong and Hendrik Santosa. Decoding four different sound-categories in the auditory cortex using functional near-infrared spectroscopy. *Hearing Research*, 333:157–166.

[25] CJ Hourdakis and A Perris. A monte carlo estimation of tissue optical properties for use in laser dosimetry. *Physics in Medicine & Biology*, 40(3):351, 1995.

[26] DM Hueber, MA Franceschini, HY Ma, Q Zhang, JR Ballesteros, S Fantini, D Wallace, V Ntziachristos, and B Chance. Non-invasive and quantitative near-infrared haemoglobin spectrometry in the piglet brain during hypoxic stress, using a frequency-domain multidistance instrument. *Physics in Medicine & Biology*, 46(1):41, 2001.

[27] Mohamad Issa, Silvia Bisconti, Ioulia Kovelman, Paul Kileny, and Gregory J Basura. Human auditory and adjacent nonauditory cerebral cortices are hypermetabolic in tinnitus as measured by functional near-infrared spectroscopy (fnirs). *Neural plasticity*, 2016, 2016.

[28] Magdy M Khalil, Jordi L Tremoleda, Tamer B Bayomy, and Willy Gsell. Molecular spect imaging: an overview. *International journal of molecular imaging*, 2011, 2011.

[29] George H Klem, Hans Otto LuÈders, HH Jasper, C Elger, et al. The ten-twenty electrode system of the international federation. *Electroencephalogr Clin Neurophysiol*, 52(3):3–6, 1999.

[30] Matthias Kohl, Christian Nolte, Hauke R Heekeren, Susanne Horst, Udo Scholz, Hellmuth Obrig, and Arno Villringer. Determination of the wavelength dependence of the differential pathlength factor from near-infrared pulse signals. *Physics in Medicine & Biology*, 43(6):1771, 1998.

www.manaraa.com

[31] Hong Yan Ma, Q. Xu, J. R. Bellesteros, Vasilis Ntziachristos, Qingqi Zhang, and Britton Chance. Quantitative study of hypoxia stress in piglet brain by IQ phase modulation oximetry. In *Optical Tomography and Spectroscopy of Tissue III*, volume 3597, pages 642–650. International Society for Optics and Photonics.

[32] Michael S Patterson, Britton Chance, and Brian C Wilson. Time resolved reflectance and transmittance for the noninvasive measurement of tissue optical properties. *Applied optics*, 28(12):2331–2336, 1989.

[33] Michael E Phelps, John C Mazziotta, and Sung-Cheng Huang. Study of cerebral function with positron computed tomography. *Journal of Cerebral Blood Flow & Metabolism*, 2(2):113–162, 1982.

[34] David Poeppel. A critical review of pet studies of phonological processing. *Brain and language*, 55(3):317–351, 1996.

[35] SA Prahl, IA Vitkin, U Bruggemann, BC Wilson, and RR Anderson. Determination of optical properties of turbid media using pulsed photothermal radiometry. *Physics in Medicine & Biology*, 37(6):1203, 1992.

[36] Scott Prahl. Optical absorption of hemoglobin, tabulated molar extinction coefficient for hemoglobin in water.

[37] Felix Putze, Sebastian Hesslinger, Chun-Yu Tse, YunYing Huang, Christian Herff, Cuntai Guan, and Tanja Schultz. Hybrid fNIRS-EEG based classification of auditory and visual perception processes. *Frontiers in Neuroscience*, 8.

[38] Charles Smart Roy and Charles S Sherrington. On the regulation of the blood-supply of the brain. *The Journal of physiology*, 11(1-2):85–158, 1890.

[39] Martin Schecklmann, Anette Giani, Sara Tupak, Berthold Langguth, Vincent Raab, Thomas Polak, Csanád Várallyay, Wilma Harnisch, Martin J Herrmann, and Andreas J Fallgatter. Functional near-infrared spectroscopy to probe state-and trait-like conditions in chronic tinnitus: a proof-of-principle study. *Neural plasticity*, 2014, 2014.

[40] Lars O Svaasand, Thorsten Spott, Joshua B Fishkin, Tuan Pham, Bruce J Tromberg, and Michael W Berns. Reflectance measurements of layered media with diffuse photon-density waves: a potential tool for evaluating deep burns and subcutaneous lesions. *Physics in Medicine & Biology*, 44(3):801, 1999.

[41] Alessandro Torricelli, Davide Contini, Antonio Pifferi, Matteo Caffini, Rebecca Re, Lucia Zucchelli, and Lorenzo Spinelli. Time domain functional nirs imaging for human brain mapping. *Neuroimage*, 85:28–50, 2014.

www.manaraa.com

[42] Arno Villringer and Britton Chance. Non-invasive optical spectroscopy and imaging of human brain function. *Trends in Neurosciences*, 20(10):435–442.

[43] Ian M. Wiggins, Carly A. Anderson, Pdraig T. Kitterick, and Douglas E. H. Hartley. Speech-evoked activation in adult temporal cortex measured using functional near-infrared spectroscopy (fNIRS): Are the measurements reliable? *Hearing Research*, 339:142–154.

[44] American National Standards Institute (ANSI), American national standard for the safe use of lasers. Standard. 2007 Z136.12007. Standard.

www.manaraa.com